A MASTER THESIS

SYNERGETIC EFFECT OF ECO-FRIENDLY CARBON COMPOUNDS OVER THE METAL OXIDE AND METAL-CHALCOGENIDE FOR ENERGY STORAGE APPLICATIONS

BHATTARAI ROSHAN MANGAL

MAJOR OF ENERGY AND CHEMICAL ENGINEERING

FACULTY OF APPLIED ENERGY SYSTEM

GRADUATE SCHOOL

JEJU NATIONAL UNIVERSITY

August, 2020

SYNERGETIC EFFECT OF ECO-FRIENDLY CARBON COMPOUNDS OVER THE METAL OXIDE AND METAL-CHALCOGENIDE FOR ENERGY STORAGE APPLICATIONS

Bhattarai Roshan Mangal

(Supervised by professor Young-Sun Mok)

A thesis submitted in partial fulfillment of the requirement for the degree of

Master of Science

This thesis has been examined and approved.

Young Sun Mok

Thesis director

Professor Young Sun Mok, Chemical and Biological Engineering

Professor Ho Won Lee, Chemical and Biological Engineering

Professor Hyomin Lee, Chemical and Biological Engineering

June 2020

Major of Energy and Chemical Engineering

Plasma Application Laboratory

Faculty of Applied Energy System

Graduate School

Jeju National University

ACKNOWLEDGEMENTS

It would not have been possible to write this thesis without the help and support of many people around me, to only some of whom it is possible to mention here.

I would like to express my deep gratitude to my supervisor Prof. Young Sun Mok. This work would not have been possible to achieve without his guidance, support, and supervision. His encouragement and belief to let me handle this work throughout my master course is something I will be in debt of. Belonging to the Electrical Engineering field, this work was not the core of my study. But with his encouragement and opportunity, I got to broaden my boundary of knowledge. It has been an honor to have him as my supervisor and to have got a chance to know him in my life.

I would like to extend my deepest thanks to my senior colleague and mentor Dr. Sudhakaran M.S.P. for all the guidance, help, and support he has provided since the beginning of this journey. His presence had made my work life so much easier and fruitful.

I also like to thank my lab members Dr. Nguyen Duc Ba, Dr. Md. Mokter Hossain, Nguyen Van Toan, Gnanaselvan Gnanasekaran, Nosir Matyakubov, and Nguyễn Hoàng Tùng for their support and encouragement throughout my master course.

Special thanks to Dr. Anil Kumar Khambampati, Dr. Rai Suresh, Dr. Pradeep Adhikari, Sunam Kumar Sharma, Maniram Banjade, and Amrita Khanal. Their invaluable suggestions, guidance, help, and support means a lot to me. Also, I am indebted to Sarbagya Maharjan and his wife Suh Hee Sook who always provided a home to go in Jeju and showered me with their kindness and care. Their presence means a lot to me and I will always be thankful to them.

I am lucky to have friends at Jeju National University who always made me feel like home. My heartiest thanks to all my friends from Vietnam, Sri Lanka, India, Bangladesh, and Pakistan. I am grateful to the staffs of the Department of Chemical and Biological Engineering for all the help regarding official issues.

It is my great honor to have been a Brain Korea 21plus Project (BK21+) scholar under the Korean Government who provided kind and generous financial assistance to carry out my study.

Finally, words will never be enough to thank my parents, brother, and in-laws. Their love and support have been the pillar to the dreams of mine. And final but extraordinary thanks to my beloved wife, Saud Shirjana, without her love, affection, and patient, I would be lost. She is the woman behind my achievement.

TABLE OF CONTENT

LIST OF ABBREVIATIONS

AC	Activated Carbon
CMC	Carboxymethyl Cellulose
CMO-GC	Cobalt Molybdenum- Glucose
CMO-NF	Cobalt Molybdenum- Nickel Foam
CV	Cyclic Voltammetry
DI	De-Ionized
EC	Electrochemical Capacitor
EDLC	Electric Double Layer Capacitor
EDS	Energy Dispersive Spectroscopy Analysis
EIS	Electrochemical Impedance Spectroscopy
ES	Energy Storage
EV	Electric Vehicle
FE-SEM	Field-Emission Scanning Electron Microscope
GCD	Galvanostatic Charge-Discharge
JCPDS	Joint Committee on Powder Diffraction Standard
LCO	Lithium Cobalt Oxide
LFP	Lithium Iron Phosphate
LIB	Lithium-Ion Battery
LMO	Lithium Manganese Oxide
LTO	Lithium Titanium Oxide
NCA	Nickel Cobalt Aluminum
NEC	Nippon Electric Company
NF	Nickel Foam
NMC	Nickel Manganese Cobalt
NMP	N-Methyl-2-Pyrrolidinone

NP	Nanoparticles
OCV	Open-Circuit Voltage
PP	Polypropylene
PVDF	Polyvinylidene Fluoride
SEI	Solid Electrolyte Interface
XPS	X-Ray Photoelectron Spectroscopy
XRD	X-Ray Diffraction

LIST OF FIGURES

LIST OF TABLES

ABSTRACT

Reducing fossil fuel consumption to help the planet gain its deteriorated health back will be the major goal for researchers in this century. Switching to greener energy sources such as solar, wind, hydro, etc. is one of the most viable options to cut down fossil fuel consumption. However, efficient storing mechanisms, as well as the conversion of the energy obtained from the aforementioned sources, is a vital part of the whole green energy solution. Systems for electrochemical energy storage and conversion include batteries, fuel cells, and electrochemical capacitors (ECs).

In recent years much attention has been given towards electrochemical capacitors, also known as supercapacitors or ultracapacitors. The engrossment of ECs is because of their attractive specifications such as high-power density, long cycle life, and hybrid nature, that bridge the gap between traditional dielectric capacitors and batteries or fuel cells. In general, according to their charge storage mechanism, supercapacitors are divided into two types: Electric Double-Layer Capacitors (EDLCs) and Pseudocapacitors. Because of the ability of pseudocapacitive materials to store charge in a faradic or redox-type process like batteries, they possess higher energy density compared to EDLCs. Hence extensive research has been focused on the synthesis and fabrication of pseudocapacitive materials.

On the other hand, due to their high energy density, low self-discharge, lightweight, and various other features, lithium-ion batteries are the most sought-after energy storage device for the verity of applications such as electric vehicles and uncountable electronic accessories for a few decades now. Conventional Li-ion batteries (LIBs) use graphite as an anode material. Graphite with a theoretical specific capacity of 372 mAh/g may no longer fulfill the tremendous energy demand of

numerous applications in imminent future. Over the past few decades, a worldwide effort has been made to search for alternative anode materials for improving the capacity and cyclability of LIBs.

The first half of this thesis work is focused on the synthesis of the pseudocapacitive material, and its practical realization as a supercapacitor device. The other half focused on the synthesis of anode material for LIBs and studied the characteristic of its energy storage by constructing CR2032 coin cells. Supercapacitor electrode was fabricated by growing $CoMoO_4$ nanoplates in the nickel foam substrate, and its pseudocapacitive properties were studied. The specific capacity of 580 F/g was obtained at the current density of the 1 A/g. Glucose was introduced as a carbon precursor to elevate the performance of the aforementioned electrode. The specific capacitance of 1638 F/g was obtained from the glucose treated electrode. Additionally, the carbonaceous electrode performed as an excellent supercapacitor device with 87% capacity retention even after 5000 charge-discharge cycles.

On the other hand, cobalt molybdenum sulfide (CoMoS) was synthesized as a novel anode material for LIBs. The CR2032 coin cells were prepared to observe the energy storage characteristics and specific capacity of as-synthesized material. In addition, dopamine was used as a carbon precursor to enhance the performance of the pristine CoMoS. The discharge capacity of 425 mAh/g and 723 mAh/g was obtained from pristine CoMoS, and carbon treated CoMoS, respectively, even after the 100 charge-discharge cycles at a current density of 200 mA/g. Furthermore, both electrodes registered excellent capacity retention ability when subjected to different current densities. In addition to the better electrochemical performance of CoMoS than the traditional graphite, the use of dopamine as a carbon source also increased its

performance in each electrochemical test and hence presented itself as a strong LIBs anode material candidate.

1. INTRODUCTION

As human civilization is moving towards the latter half of the first quarter of the 21st century, global warming remains a topmost threat for planets sustainability. From the starting of the industrial era until now, the main reason for global warming is greenhouse gases such as CO_2, CH_4, NO_s, etc. Greenhouse gases that keep the planet warm and habitable can make it completely barren, too, if increased above a certain limit. Major sources of greenhouse gas emissions are transportation, electricity production, and industry [1–4]. If we compartmentalized the greenhouse gases with their sources, we could think of a way to cut back the emission. Fossil fuel burning is almost the sole reason for the human-induced greenhouse gases. Reduction in fossil fuel consumption to help the planet gain its deteriorated health back will be the major goal for researchers in the coming decades. Switching to greener energy sources such as solar, wind, hydro, etc. is one of the most viable options to cut down fossil fuel consumption. Solar and wind are the energy sources that we have in abundance and might last for thousands of years in the future. The conversion and storage of the energy obtained from these sources is a vital part of the whole green energy solution. It is hard to predict the energy demand of any consumer at any time of the day; hence the proper storage of energy produced from greener sources is an important task. Recent advancement in the electric vehicles research and development has sparked a ray of hope that a large portion of greenhouse gas emission could be cut off, which is produced from the transportation sector. But as a portable nature of the vehicles, the most basic job for the better electric vehicle is the invention of proper portable energy sources. Not only the electric vehicle but the uncountable electronic devices that we use in our daily life demand the portable energy sources. For example, more than 85% of the world

population has access to the most basic electronic device, a mobile phone [5]. All these arguments suggest that the most basic mandate of the energy source is portability. This basic nature of demand gave birth to some exceptional systems for energy storage (ES) and conversion, which are batteries, fuel cells, and electrochemical capacitors (ECs). These systems store energy in the form of chemical energy and can deliver the stored energy in the form of electrical energy. Hence, they are also referred to as electrochemical energy storage devices [6–8]. These different ES systems can be compared together in terms of their energy and power values by a plot called Ragone plot.

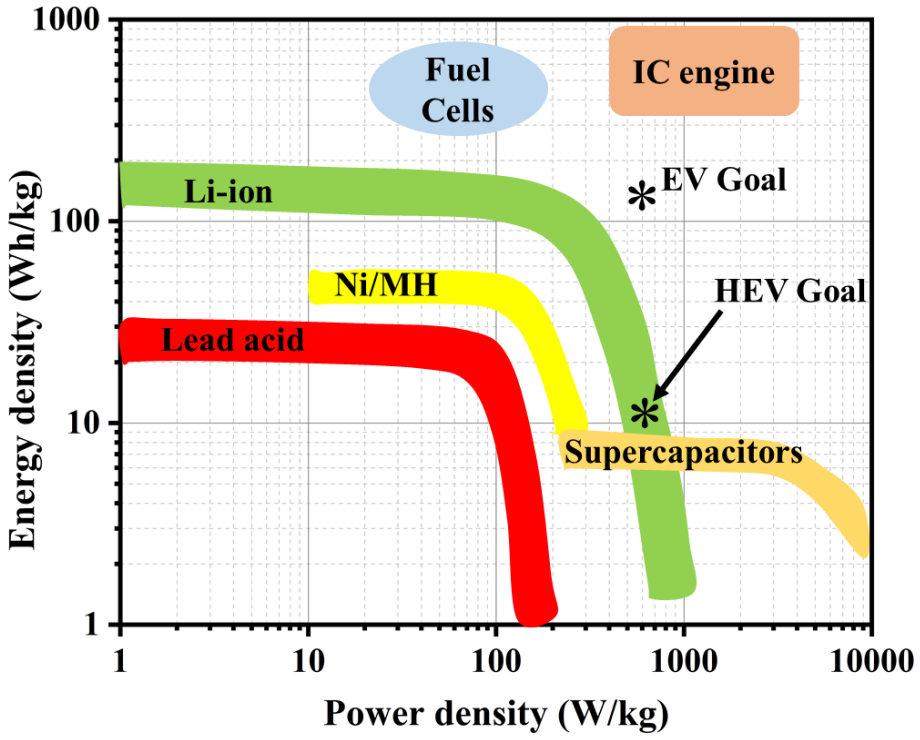

Figure 1.1 Ragone plot for different energy storage devices.

Figure 1.1 shows the Ragone plot of different ES devices with their respective specific energy and specific power plotted on the logarithmic scale [9–11]. As we can see in the figure, the batteries lead capacitors with higher specific energy, whereas

capacitor leads batteries with higher power density. To fabricate a device that possesses a specific capacity of the battery and specific power of capacitors would be the ideal finding. In this thesis work, battery and electrochemical capacitors are going to be discussed, and we will aim to improve the electrochemical performance of the said ES applications.

1.1. Battery

A battery is a device that stores energy in the form of chemical energy. It can convert the stored energy to the electrical energy by faradic oxidation and reduction reactions that happen in its electrodes [6, 12]. Batteries can be classified into many groups depending on their usages such as their working property: rechargeable or non-rechargeable, their build property: aqueous or non-aqueous, liquid, or solid electrolyte, their working conditions: low or high temperature, etc.

A battery is composed of three components:

1. The positive electrode (cathode): the electrode that gets reduced during an electrochemical reaction.
2. The negative electrode (anode): the electrode that gets oxidized during an electrochemical reaction.
3. Electrolyte: the conductive medium between anode and cathode, which helps to transfer the ions during oxidation and reduction reactions.

The important point to consider here is, all the battery component terminologies are defined with the supposition that they are inside the primary battery. That is, only the discharge process is happening. In terms of a secondary battery, the cathode and anode electrode changes according to the charging or discharging of the battery. Here

we will discuss the secondary batteries only, owing to the simple fact that secondary battery can be used for many charge-discharge cycles and hence considered to be the future of the ES system.

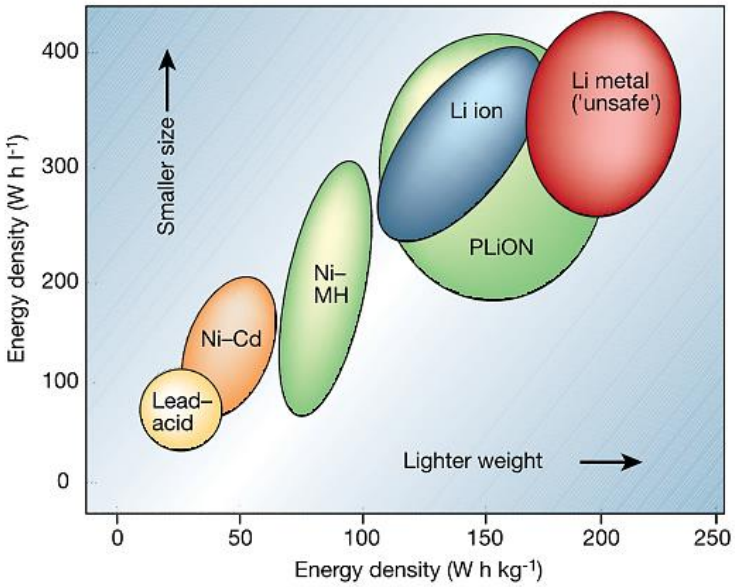

Figure 1.2 Comparison of different battery systems to their energy density.

Figure 1.2 shows different types of batteries compared to their volumetric and gravimetric energy densities [13, 14]. With a molecular weight of 6.941 g/mol and density 0.51 g/cm^3, lithium is among the lightest metal. Despite being light and small, it packed a higher amount of energy compared with any other battery combinations. As we can see in the figure, the lithium-ion batteries (LIBs) lead the battery ES system with its superior volumetric as well as gravimetric energy density. In addition to the high energy and power density, LIBs possess the theoretical specific capacity of as high as 3860 mAh/g and is also considered to be the most electropositive element in nature [15, 16]. This feature of LIBs makes it the most attractive ES system for a variety of applications such as portable electronics and EVs. Hence this thesis work will be focused mainly on LIBs and its peripherals. The work done to improve the efficiency

of LIB using various experimental techniques will be presented in the forthcoming chapters.

1.2. Electrochemical capacitor

Conventional capacitors are known to compose of positive and negative electrodes separated by an electrically non-conductive dielectric medium. In these capacitors, the dielectric separator would help to accumulate the charge on the electrode surface by the dipole polarization. Another type of capacitor has the liquid or solid medium in between the electrode plates, which is often called the electrolyte. These capacitors are collectively known as an electrochemical capacitor (EC). Unlike in the dielectric medium, this type of capacitor accumulates the charge in the electrode surface by the ionic movement through the electrolyte medium. In the conventional capacitors, the charge accumulation in the electrode surface is always limited by the adjacent dipoles. On the other hand, for ECs, the ions can roam freely in the electrolytic medium. So the amount of charge accumulation and hence the capacitance of these capacitors is much higher than that of the conventional capacitors[17–19]. Owing to their excellent charge storage property, the ECs are often mentioned as supercapacitors, ultracapacitors, double-layer capacitors, power capacitors, etc. [20]. Henceforth we will refer them as an electrochemical supercapacitor or in short ‘supercapacitor’. In recent years much attention has been given towards supercapacitor because of their attractive specifications such as high power density, long cycle life, and hybrid nature that bridge up the gap between traditional dielectric capacitors and batteries or fuel cells [21, 22] Depending on their approach of energy storage and construction mechanism, supercapacitors are mainly divided into three types:

1.2.1. Electric double-layer capacitors

The energy storage mechanism of EDLCs is much like that of traditional electrolytic capacitors i.e. by charge separation. The capacitance in EDLCs arises from the charges which are physically stored on the surface of the electrode. The adsorption-desorption mechanism of charged ions from an electrolyte forms a double layer structure on the electrode surface with the oppositely polarized electrode ions [23]. The ion layers are separated by a single layer of electrolyte molecules on both positive and negative electrodes. This phenomenon gives rise to double layers capacitors in each electrode and hence the name was given as Electric Double Layer [22, 24, 25]. There is no faradic reaction involved in the EDLC electrodes and hence no phase change of the active material takes place. Because of this fact, EDLCs can sustain thousands of more charge-discharge cycles than batteries [26]. Despite higher charge-discharge cycling ability, these ECs are bound by the surface charge store mechanism which limits the energy density of the supercapacitor device. EDLCs usages carbon-based electrode materials with a high surface area. Some of the leading electrode materials for the EDLCs are carbon nanotubes, graphene, activated carbon, carbon aerogels, carbon foams, carbide-derived carbon, etc. [27].

1.2.2. Pseudocapacitors

In the case of EDLCs, the ions would cling to the surface of the oppositely polarized electrode, whereas for pseudocapacitors some of those ions penetrate through the single electrolyte molecules layer between the ion electrode interface and adsorbed to the electrode surface. The adsorbed ions donate an electron to the electrode materials which are often the electron-deficient transitional metal oxides and gives rise to the faradic current. The capacitance originated from this faradic charge transfer

phenomenon is referred to as pseudocapacitance [28–30]. Because of the ability of pseudocapacitive materials to store charge in a faradic or redox-type process similar to batteries, they possess higher energy density compared to EDLCs, and hence extensive research has been focused on synthesis and fabrication of pseudocapacitive materials [31, 32]. Despite the higher energy density, the phase changes within the electrode due to the faradic reaction limits the cyclability and power density of the pseudocapacitors [33]. Two types of electrode materials are extensively studied for pseudocapacitive energy storage, conducting polymer-based pseudocapacitors [34, 35] and metal oxide-based pseudocapacitors such as Ruthenium Oxide [36, 37]. For the materials to be a pseudocapacitive they must possess basic EDLC-type electrochemical features [29].

1.2.3. Hybrid supercapacitors

The concept of hybrid supercapacitors is to eliminate the shortcomings of EDLCs and pseudocapacitors while preserving their best features. Hybrid supercapacitor offers synergic behavior and improved properties with respect to their individual components [38]. Various hybrid supercapacitor systems have been designed by combining the redox (battery type) electrode such as metal oxides or conducting polymers with an activated carbon electrode [39, 40]. The redox electrode increases the energy density of the device which is complemented by the capacitive electrode that ensures the high-power density. Depending on the electrode configurations, hybrid capacitors are divided into three types as composite, asymmetric, and battery type [27, 41]. Although debates are going on about the correct way of grouping the hybrid supercapacitors [29], these three types cover all the known researches done on hybrid supercapacitors.

A) Asymmetric

The asymmetric hybrid supercapacitor uses two different types of electrodes to form a supercapacitor device. Generally, one electrode is pseudocapacitive of nature and another is EDLC in nature. Coupling these electrodes usually increases the potential window of the device and hence increases the energy density. Some of the well-known material combinations on asymmetric supercapacitors are conducting polymers positive electrode and activated carbon negative electrode[42, 43].

B) Composite

As the name suggests, the composite electrodes combine the carbonaceous material with pseudocapacitive material. As a result of this combination, the carbonaceous material facilitates the charge transferability of the pseudocapacitive material and also increases the effective surface area of the electrode. Whereas pseudocapacitive material increases the energy density of the composite. The composite, in turn, provides the energy density and cyclability higher than the pristine pseudocapacitive electrode and carbon EDLC electrode individually would provide[44, 45].

C) Battery-type

Battery-type supercapacitor also combines two different types of electrodes to improve device efficiency. However, the important prospect here is one electrode must be composed of battery type material unlike asymmetric hybrid devices, where both electrodes are capacitive of nature. In battery type hybrid device the capacitive electrode used can either be EDLC or pseudocapacitive of nature and can be used either as a cathode or anode material[46]. Also, it is noteworthy to mention that we are

discussing the internal hybridization of battery and supercapacitor system, rather than the physical coupling of already built battery and supercapacitors. Similar to the other two hybrid supercapacitors here also a redox reaction happens at battery type electrode and ion accumulation or rapid charge transfer happens at the capacitive electrode. The use of battery type material opens up a huge possible combination of materials that can be used in this type of hybrid device.

Another chapter of the thesis work is focused on the fabrication of a supercapacitor hybrid device that exploits all three hybridization techniques and improves its energy density and cyclability.

2. LITERATURE SURVEY

2.1. Battery

As discussed earlier, lithium-Ion Batteries (LIBs) have been a major energy source for uncountable electronic accessories including EVs for some time now[47–51]. Because of the intense and very well-spread use of the li-ion battery, it is now a very important job for researchers and scientists to improve their cost and performance which in return greatly expands their applications and enables new technologies that depend on energy storage. Research and development work on lithium battery goes back to as early as the 1970s when M. Stanley Whittingham developed a lithium metal battery with titanium(IV) sulfide and lithium metal as an anode and cathode electrodes respectively [52, 53]. However successful commercialization of the LIBs started from 1991 only, when Sony starts to manufacture them with $LiCoO_2$ (LCO) as a cathode and graphitic carbon as an anode electrode, employing the findings of JB Goodenough and team [54]. Even after almost three decades, the same LIB electrode configuration is dominating an ES device market. Particularly because of the attractive features of LCO such as its relatively high theoretical specific capacity of 274 mAh/g, the high theoretical volumetric capacity of 1363 mAh/cm^3, low self-discharge, high discharge voltage, and good cyclic performance [55, 56]. However, because of the high cost of cobalt, LCO electrodes are quite expensive and limit its practical usability in ES applications. Besides, low thermal stability and capacity fade at high current rates also hinders its performance [57]. As a result, in the quest of developing cheaper and efficient cathode electrode for LIB, different material configurations were developed, and successful commercialization also achieved. Some of the well-known cathode material configurations are transition metal oxides such as $LiNi_{0.8}Co_{0.15}Al_{0.05}O_2$ (NCA)

[58], $LiMnO_2$ (LMO) [59], $LiNi_xCo_yMn_zO2$ (NMC) [60] and polyanion compounds such as $LiFePO_4$ (LFP)[61].

On the other hand, LIBs widely use graphitic carbons and hard carbons as an anode material. Intercalation of Li-ion in the graphene planes gives rise to the electrochemical activity needed for an energy storage application [62]. Many superior properties such as mechanical stability, electrical conductivity, low cost, abundant availability, low delithiation potential vs Li, high Li diffusivity makes carbon a very favorable anode electrode material. $Li_4Ti_5O_{12}$ (LTO) is another anode material that has been successfully commercialized and extensively used in many ES applications. Few advantages of LTO over graphitic anode are lower self-heating with respect to graphite, heat generation at elevated temperature is less than graphite, can absorb O_2 from cathode thus increasing the stability of cell, and calendar life estimated to be 20+ years [62]. However, carbon anode with a theoretical specific capacity of 372 mAh/g and LTO with specific capacity of 175 mAh/g may no longer fulfill the LIBs energy demand from numerous power grasping applications [63].Over the past few decades, a worldwide effort has been made to search for alternative anode materials for improving the capacity and cyclability of LIBs[9, 64, 65].

Transitional metal sulfides have been extensively studied as an alternative anode material that could potentially replace graphite mainly because of their high theoretical capacity, natural abundancy, low volumetric expansion upon lithiation de-lithiation cycles [66, 67]. Especially layered metal chalcogenides where the atoms are covalently bonded to form two-dimensional (2D) layers that are stacked together through weak van der Waals interactions are reported to possess excellent ability to withstand the volume expansion and hence the greater cyclability as LIB materials [68–

72]. Molybdenum sulfide in particular with its layered structure possesses a theoretical capacity of around 669 mAh/g and has been seen as an excellent LIBs anode material [73, 74, 75]. However poor cyclability and low electrical conductivity hinder its otherwise excellent features [76, 77]. On the other hand, cobalt sulfide with its higher electronic conductivity and thermal stability has been considered as another excellent LIBs anode material [78, 79]. However, similar to molybdenum sulfide, cobalt sulfide also suffer from the pulverization caused by the volume change upon many cycles [80]. Various stoichiometric compositions such as CoS [81], CoS2[77], Co3S4[82], etc were prepared and reported to tackle the problems arises from volume expansion. But still, no definite outcome has achieved and there is a lot of room for improvement. Another way to enhance the properties of cobalt and molybdenum sulfides would be to combine them and prepare a ternary metal sulfide. Doing so would increase the electronic conductivity of the composite and also provide an additional redox reaction species which can improve the electrochemical performance of the ES device [83, 84]. Combining cobalt and molybdenum sulfides in an attempt to extract the best out of their features has long been practiced in electrocatalytic reactions[85–88]. However, only a few reports are there of cobalt, molybdenum, and sulfur composite as an ES device, such as CoMoS composite for LIBs and SIBs [89–91] or supercapacitor[92–95].

Furthermore, making a composite of battery active materials with carbon has long been in practice and proved to improve the ES device performance. Dopamine has been reported as a nitrogen-doped carbon-rich precursor for a verity of applications [96–99]. The self-polymerization ability of dopamine that enables it to stick to virtually any surface regardless of their chemical nature proved to be very efficient and cost saving[100–102]. The porous morphology and multilayer graphene-like structure of dopamine have an electrical conductivity close to that of N-doped graphene[103, 104].

These attractive features make this an excellent carbon precursor in the energy storage ecosystem and rightly so it has been incorporated in various energy storage devices such as LIBs and supercapacitors[104–108].

We adopt a simple one-pot hydrothermal method to synthesize the $CoMoO_4$ nanorods. The CoMoS composite was prepared by a solid-phase reaction of $CoMoO_4$ and thioacetamide. The self-polymerization ability of dopamine was employed to synthesize nitrogen-doped cobalt molybdenum sulfide CoMoS@NC. The polydopamine layer on the CoMoS nanocomposites functioned as buffering and conducting matrix that restricted the volume change and enhanced the electronic conductivity of the electrode material and hence the specific capacity of the Li/CoMoS@NC half-cell.

2.2. Supercapacitor

The capacitors have been around since the mid of 18^{th} century. Whereas the ultracapacitors come almost after 100 years. The ultracapacitor technology was first patented by Standard Oil in 1966 [109]. The successful commercial production of supercapacitors starts from 1971 licensed by the Nippon Electric Company (NEC) [110]. These supercapacitors employ the high surface area activated carbon fibers over the metallic current collector plates. As discussed earlier, depending on their approach of energy storage and construction mechanism, supercapacitors are mainly divided into three types, electric double-layer capacitors (EDLC), Pseudocapacitors, and hybrid supercapacitors. It is also explained in the previous chapter in detail why recent research is focused on pseudocapacitors and hybrid supercapacitors.

Transition metal oxides with their high specific capacitance and low resistance are an excellent candidate for the pseudocapacitive supercapacitor material. A substantial amount of research has been done on transition metal oxide as a supercapacitor materials such as $RuO_2.xH_2O$ [111], MnO_2 [112, 113], Nickel Oxides [114], V_2O_5 [115] owing to their high theoretical specific capacitance, low cost, abundance in nature as well as the environment-friendly nature[116]. Recently as a low-cost alternative to single metal oxides, binary metal oxides such as $NiCo_2O_4$[117], $ZnCo_2O_4$[118], Zn_2SnO_4[119], etc. are perceiving as a viable option. With different oxidation state materials that enable multiple redox reactions and higher electrical conductivities, these metal oxides have been widely studied[120].

Cobalt molybdate has been proved as an excellent candidate for supercapacitor mainly because of its high theoretical specific capacitance and great redox activity[121]. However, because of its low experimental capacitance value and poor rate capability, the research has been focused on how to improve the mentioned shortcomings of this material. Few effective methods in practice so far are sophisticated approaches such as incorporating the cobalt molybdate nanoparticles in 3-D graphene structures[122, 123] or combining two or more metal oxides to form a structure with higher specific capacitance, which also is more resilient to continuous charge-discharge [116, 124–126].

Glucose has been used in a variety of fields due to its unique properties such as eco-friendly, abundant resources, low carbonization temperature, and low cost.[127, 128]. It has been reported to be used as an ideal catalyst supports for fuel cells [129], as a facilitator in an immunoassay process in medicine [130], and many more. The use of glucose in the supercapacitor ecosystem is mainly as an element in a carbonaceous

electrode to increase the conductivity by increasing the porosity of the carbon source. Also, to improve the stability and contact between the current collector and active material and hence improving the electrochemical performance of the system. The main merit of bio-mass derived carbon compounds is the possibility of altering the physical and chemical properties resulting in more electroactive material.[131–133]

In this work, we focus on the effect of the incorporation of glucose-derived carbon by the systematic formation of nanosized carbon by the facile hydrothermal method. Glucose is abundant and renewable biomass with a rich hydroxyl functional group. Consequently, the embedded carbon enhances the experimental specific capacitance of the cobalt molybdate. Considerably basic experimental steps were followed, and some outstanding results were obtained provided such simple procedures.

3. MATERIALS AND METHODOLOGY

3.1. Chemicals and gases

Various chemical compounds were used throughout the different experiments. Several protective measures were practiced while handling the chemicals. All chemicals used in the process were of research-grade and were used as they arrived without further purification. The table below consist of all the chemicals used in this study:

Table 3.1 Chemicals used in the study.

Chemical	Formula	Purity	Vendor	Usages
Cobalt Nitrate	$Co(No_3)_2.6H_2O$	98%	Junsei Chemical Co. Ltd., Japan	Cobalt precursor
Carboxymethyl cellulose (CMC)	-	-	Junsei Chemical Co. Ltd., Japan	Battery slurry binder
Dopamine hydrochloride	-	-	Sigma Aldrich, Germany	Carbon precursor
Ethanol	C_2H_5OH	99.5%	Daejung Chemicals & Metals Co. Ltd., South Korea	Cleaning solvent
Glucose	$C_6H_{12}O_6$	99%	Alfa Aesar, England	Carbon precursor
Hydrochloric acid	HCl	35%	Daejung Chemicals & Metals Co. Ltd., South Korea	Cleaning solvent
Lithium foil	Li	-	HONJO METAL CO., LTD., Japan	Battery electrode
Lithium hexafluorophosphate in EC/DEC	$LiPF_6$	-	Sigma Aldrich, Germany	Battery electrolyte

Nickel foam	Ni	-	MTI Corp., Ltd., South Korea	Current collector for supercapacitor
Potassium hydroxide	KOH	93%	Daejung Chemicals & Metals Co. Ltd., South Korea	Supercapacitor electrolyte
Sodium molybdate	$Na_2MoO_4.2H_2O$	98.5%	Junsei Chemical Co. Ltd., Japan	Molybdenum precursor
Thioacetamide	C_2H_5NS	98%	Wako Pure Chemicals, Japan	Sulfur precursor
Tris buffer	-	99%	Alfa Aesar, China	pH buffer

The gases used in the study are also tabulated as below:

Table 3.2 Gases used in the study.

Gases	Formula	Purity	Vendors	Usages
Argon	Ar	99.9%	P. S. CHEM CO., LTD	The inert atmosphere for chemical compound synthesis
Standard Gas Mixture	H_2:10% Ar: Balanced	-	P. S. CHEM CO., LTD	Regeneration of the glove box
UHP Argon	Ar	99.999%	P. S. CHEM CO., LTD	The inert atmosphere for the glove box

3.2. Apparatus

Instruments and apparatus used for the study are given below.

Table 3.3 Apparatus used in the study.

Apparatus	Specification	Manufacturer
Autoclave	PTFE Container	Latech
Balance	DRAGON 204/5	Mettler Toledo

Battery test station	PESC05-0.1	PNESOLUTION CO., LTD. South Korea
Cell punching tool	WA-1006	Wellcos corporation, South Korea
Centrifuge	LABOGEN-1580	GYROZEN Co., Ltd., South Korea
Coin cell crimper	HSMCC-P10	Wellcos corporation, South Korea
Electrochemical workstation	AUTOLAB PGSTAT302N	ECO Chemie
Furnace	DFT-50300	DH Science
Glove box	2 persons (4 port)	M.O. Tech, South Korea
Hot plate and magnetic stirrer	MGH-320	SIBATA
Incubator	JSBI-100C	JS RESEARCH INC., South Korea
Oven	LDO-030N	DAIHAN LABTECH CO., LTD., South Korea
Oven (vacuum)	JSVO-30T	JS RESEARCH INC., South Korea
Ultrasonicator	JAC-4020	KODO, South Korea

3.3. Materials syntheses

For the electrochemical ES devices, the structure of the active material plays a significant role in their performance. Nanomaterials with uniform size and distribution are much desired for the optimum performance of the ES device. Here, some of the well-known material synthesis approaches were practiced producing nanomaterials with the desired shape, size, and distribution. The material synthesis methods implemented are as follows,

3.3.1. Hydrothermal synthesis

Hydrothermal synthesis incorporates the high temperature and high pressure in an aqueous medium to synthesize the different shapes and sizes of nanoparticles. Generally, Teflon-lined autoclaves are used as a container because of their ability to work under high temperature and pressure, as well as alkaline media [134]. In a typical procedure, the reactants are placed inside the Teflon-lined steel autoclave and kept in an oven at the temperature well above the boiling points of the solvents where the solvent reacts as supercritical fluids. Which, in turn, increases the solvent's ability to dissolve the solid and hence increases the reaction speed [135]. The hydrothermal synthesis has lots of advantages such as fast reaction kinetics, short processing times, phase purity, high crystallinity, high yield, homogeneous particle products, composite formation, narrow particle-size distributions, and is cost-effective, environment friendly, and easily scalable [136]. In this study, the hydrothermal synthesis was used to synthesize the $CoMoO_4$ nanopowder and self-grown $CoMoO_4$ nanoplates on a nickel substrate.

3.3.2. Solid-state reaction

As the name suggests, the solid-state reaction is essentially the reaction between two solids to form one or more product phases. The solid-state reaction is a straightforward and cost-effective method that favors the synthesis of a product with a highly amorphous nature [137, 138]. In this study, cobalt molybdenum sulfide was synthesized by the solid-state reaction between cobalt molybdate and thioacetamide nanopowders.

3.4. Material characterizations

3.4.1. X-ray diffraction (XRD) analysis

XRD is the experimental technique used to determine the molecular structure, phase purity, size, and much more information about the crystal. The basic principle relies on the fact that when a beam of an x-ray with fixed wavelength is incident on crystal planes, the electrons within the atoms of the crystal reflect the incident waves. These reflected waves scatter in many directions, and most of them cancel each other through destructive interference. However, some of them add up and travel in a specific direction through constructive interference. For the constructive interference to occur some specific parameters should be fulfilled, which is demonstrated by the brags law as,

$$n\lambda = 2d\sin\theta \quad \ldots\ldots (1)$$

Where n is the order of reflection, λ is the wavelength of the incident x-rays, d is the interplanar spacing of the crystal, and θ is the angle of incident. Constructive interference will occur only for a combination of that specific wavelength, crystal lattice planar spacing, and angle of incidence. For a given XRD analysis, the known variables are n, θ, and λ, and by solving equation 1 for d, we can verify the unknown crystal as all the crystals are composed of numerous planes with unique planer distance. For this study, we used the PANanalytical's Empyrean XRD with Cu Kα (λ = 0.15405 nm) radiation in the scan range (2θ) of 5° to 80°.

3.4.2. Field-emission scanning electron microscope (FE-SEM)

FE-SEM is used to get a visual idea about surface topography and morphology, such as the shape and size of the sample in nanoscale. A focused beam of an electron that interacts with the sample atoms is used to produce the image. For this study, we used the TESCAN, MIRA3 FE-SEM instrument. The samples were coated with platinum or carbon depending on their nature before the SEM analysis.

3.4.3. Energy dispersive spectroscopy analysis (EDS)

EDS was used to verify the elemental composition and to estimate their relative abundance on the prepared sample. The basic principle of EDS is that each element has a unique atomic structure that allows a unique set of peaks on its electromagnetic emission spectrum. Typically EDS instrument measures the difference in energy spectrum between the higher and lowers energy shell electron when the higher energy shell electron moves to a lower energy shell [139]. For our study, EDS was done with TESCAN, MIRA3 FE-SEM instrument with a separate EDS detector (INCA) connected to the FE-SEM instrument.

3.4.4. X-ray photoelectron spectroscopy (XPS)

The chemical composition and the state of elements present in the outermost part of the sample were obtained by XPS analysis. The ESCA-2000, VG Microtech Ltd, and Theta Probe AR-XPS system (Thermo Fisher Scientific, U.K). Here a monochromatic X-ray beam source at 1486.6 eV (Aluminum anode) and 14 kV was used to scan the sample surface. A high flux x-ray source with aluminum anode was used for x-ray generation, and quartz crystal monochromatic was used to focus and scan the x-ray beam on the sample.

3.5. Electrode and ES device fabrication

3.5.1. Supercapacitor electrode and device

The positive working electrode was prepared by a self-grown method and electrochemically characterized on a three-electrode system individually. In a typical process, a nickel foam (1×1 cm^2) was first cleaned with 6M HCl to remove the oxide layers present on the surface. The cleaned nickel foam was then used to grow the active material ($CoMoO_4$) by a hydrothermal method. The detailed mechanism and precursor used are also discussed in the material synthesis part of the respective chapter. The negative working electrode was prepared by a slurry coating method. In a typical process, the active material (activated carbon) was mixed with a PVDF, Super P, and NMP to make a slurry. The slurry was then coated on a cleaned Ni foam, as mentioned earlier. Both positive and negative electrodes were studied for their respective electrochemical properties. The hybrid supercapacitor device was prepared by combining the positive and negative electrode with polypropylene separator in between them.

3.5.2. LIB electrode and device

A slurry coating process was used to prepare the lithium-ion battery electrode. In a typical process, the active material ($CoMoO_4$) was mixed with carboxymethyl cellulose (CMC) and super P in the ratio of 70:15:15 with water as a solvent. The detailed mechanism and respective amounts of the material used are discussed in the respective chapter. The properly mixed slurry was then coated on a copper foil and dried in a vacuum oven. The obtained copper foil with an active material was punched with 12 cm dia to prepare an electrode. CR2032 half-cell was prepared inside a glove

box with the as-prepared electrode as a working electrode and metallic lithium foil (16 cm^2 dia) as a counter as well as the reference electrode. As fabricated coin cell was checked in a battery testing system for various electrochemical properties.

3.6. Electrochemical characterizations

The electrodes and devices prepared, as mentioned earlier, are characterized using various techniques to determine their respective properties and to monitor their performance as a practical energy storage application. For the supercapacitor, electrochemical characterization was performed in a three-electrode system, the Ni foam with active material as a working electrode, a platinum foil (0.8×0.8 cm^2) as a counter electrode and an Ag/AgCl electrode as a reference electrode. As an electrolyte, 2 M aqueous KOH solution was used. The room temperature was kept constant throughout the study. In the case of LIB battery coin cells, the coin cell holder was kept inside an incubation chamber, and the temperature was always maintained at 25° C. Different approaches implemented for the characterization of the electrodes and devices are discussed below.

3.6.1. Cyclic voltammetry (CV)

Cyclic voltammetry is commonly used to investigate the reduction and oxidation processes of the elements present in the working electrode by plotting the potential applied in the x-axis and current induced in the x-axis [140]. The potential of the working electrode is controlled versus the reference electrode (Ag/AgCl for this study), and a voltammogram is obtained by measuring the current at the working electrode during the potential scan [141]. The CV plot can also be used to differentiate between the EDLC, pseudocapacitive, or battery type material according to the nature

of the voltammogram plot obtained. Also, the charge storage reversibility of the active material can be attained by the CV plot by analyzing the nature of the plot during the positive and negative scan, and whether they look symmetrical or not. The voltammogram plotted with increasing potential scan rates gives the idea about the charge storage ability of the working electrode material during the high scan rates. For this study, the CV was performed within the scan rate from 5 mV/s to 200 mV/s and between the various potential window according to the electrode material, which is discussed in their respective chapters.

3.6.2. Galvanostatic charge-discharge (GCD)

GCD is commonly used to observe the cycle life of the working electrode by subjecting them to numerous charge and discharge cycles at a constant positive and/or negative current. The GCD plot can be obtained by plotting the potential difference data on the y-axis with the time on the x-axis. GCD profiles are used to evaluate the quality of capacitive response, identify the possible presence of irreversible Faradaic reactions, and to derive several figures, such as capacitance, capacity, energy, and power of the ES device [142]. The nature of electrode material, i.e., EDLC, pseudocapacitive, or battery type, can be determined from the GCD plot as EDLC materials give a linear. In contrast, pseudocapacitive materials give a variety of non-linear charge-discharge plots. For this study, GCD versus time and GCD versus capacity are discussed for supercapacitor and battery, respectively, and are explained in their respective chapters.

3.6.3. Electrochemical impedance spectroscopy (EIS)

EIS is the most comprehensive approach to analyze the charge transfer kinetics, such as capacitance and resistance within the various components of the electrode.

Normally, an alternating voltage is applied to the electrode over a vast range of frequency ranging from few hertz to 100 of thousands hertz and amplitude, and a phase shift of resulting current will be measured. From the EIS study, we can obtain the plot called the Nyquist plot, where the imaginary component of the impedance is plotted against the real component of impedance. The data plotted in the Nyquist plot is then fitted with equivalent mathematical models. From the fitted model, one gets an idea about the resistive and capacitive components and how they are affecting the charge transfer properties of the electrode material. Mathematical modeling of the electrodes and ES devices and their in-depth nature are discussed in the respective chapters.

3.7. Electrochemical measurements

As mentioned earlier, for a single electrode, the electrochemical measurements were performed on the three-electrode system with active material containing electrode as a working electrode, platinum as a counter electrode, and an Ag/AgCl as a reference electrode. 2M KOH was used as an electrolyte solution. The supercapacitor device was fabricated using self-grown active material as a positive and activated carbon as a negative electrode with a polypropylene separator in between them. CV, GCD, and EIS were performed for all of the mentioned electrodes and devices. The specific capacitance was calculated from the data obtained from the GCD cycles as the GCD is believed to give more accurate results because of its close resemblance with the practical applications [143].

As we know, the capacitance of an electrode in an electrochemical system is,

$$C = \frac{\Delta Q}{\Delta V} \quad \text{…..…….(2)}$$

Where, ΔQ is the charge stored, and ΔV is the potential window of the electrode. Equation 2 can be rewritten as,

$$C = \frac{i \times \Delta t}{\Delta V} \quad \text{.....(3)}$$

Where i is the applied current, and Δt is the discharge time.

Hence, the specific capacitance can be given as,

$$C_s = \frac{i * \Delta t}{m * \Delta V} \quad \text{.....(4)}$$

Where m is the mass of the active material.

Likewise, the energy density and power density of the device were calculated from the specific capacitance derived in equation 4. The governing equation for energy density and power density are as follows,

$$E = \frac{1}{2} C_s V^2 \quad \text{.....(5)}$$

Where E is the energy density of the device, C_s is the specific capacitance of the device, and V is the potential window.

$$P = \frac{E}{\Delta t} \quad \text{.....(6)}$$

Where P is the power density, E is the energy density, and Δt is the discharge time.

Following mass balance equation was used to calculate the actual mass of the activated carbon needed to fabricate a supercapacitor device,

$$\frac{m^-}{m^+} = \frac{C^+ \times \Delta V^+}{C^- \times \Delta V^-} \quad \text{…..……(7)}$$

Where, m^- is the active material mas of the negative electrode, m^+ is the active material mas of the positive electrode, C^+ is the specific capacitance of the positive electrode, C^- is the specific capacitance of the negative electrode, ΔV^+ is the potential window for the positive electrode at which the specific capacitance was calculated and ΔV^- is the potential window for the negative electrode at which the specific capacitance was calculated.

4. EXPERIMENTALS

4.1. Battery

4.1.1. Preparation of $CoMoO_4$

The previously reported method was implemented to obtain uniformly distributed $CoMoO_4$ nanorods[144]. In a typical synthesis process, 1 mmol of $Co(NO_3)_2.6H_2O$ and 1 mmol of $Na_2MoO_4.2H_2O$ were added in 80 mL solution of solvents composed of water, ethanol and diethyl glycol in the volumetric ratio of 2:1:2. The solution was stirred in magnetic stirrer for one hour then kept in 100 ml Teflon lined steel autoclave and heated at 180 degrees for 10 hours. The final solution was obtained as a pink segregate in a clear solution. The obtained solution was washed several times with ethanol and DI water and kept in a vacuum oven at 80 degrees for 8 hours to dry. Dark violet (color code: #9400d3) powder was obtained after vacuum drying. The product obtained from vacuum drying then kept in a high-temperature furnace at 400 degrees at the rate of 1 degree per minute for 3h for the final annealing process. Dark blue magenta (color code: #685580) powder was obtained after the final annealing process.

4.1.2. Preparation of CoMoS

CoMoS composite was synthesized through the direct pyrolysis of $CoMoO_4$ and thioacetamide under an inert atmosphere. In a typical process, $CoMoO_4$ powder and thioacetamide (1:3 weight ratio) were ground together for a few minutes to make a well-mixed fine powder. The mixed powder then put in the furnace at 500 degrees for 5

hours under argon atmosphere. The expected governing equation that takes place in the furnace can be summarized as,

$$CoMoO_4 + 4C_2H_5NS \rightarrow CoMoS_4 + 4C_2H_5NO \quad \ldots\ldots\ldots\ldots\ldots\ldots\ldots\ldots(8)$$

The final product obtained was in the form of a black dried solidly aggregated deposit. The final product was ground again to make the fine powder for further use and named as CoMoS.

4.1.3. Preparation of CoMoS@NC

We implemented the self-polymerization ability of dopamine to form a very thin carbon film on CoMoS nanoparticles. In a typical process 0.1mM of tris buffer solution was prepared on DI water separately. The tris buffer solution was added on 400ml DI water dropwise to maintain the pH of the solution to slightly higher than 8.5. 200mg of CoMoS was dispersed on tris buffer adjusted solution and left to sonicate for one hour. After the sonication, 100mg dopamine hydrochloride was added into the solution and left to stir overnight in a magnetic stirrer. The dark black solution obtained after stirring was washed with DI water for a few times and then with ethanol. The final black compound was kept in a vacuum oven at 80 degrees for drying. Vacuum dried black compound was kept in a furnace at 500 degrees for 4 hours at 3 degrees/min under argon atmosphere for calcination. The final black powder obtained was named as CoMoS@NC.

4.2. Supercapacitor

4.2.1. Growing $CoMoO_4$ on nickel foam

Before proceeding forward, nickel foam (NF) was treated with hydrochloric acid to remove any oxide layers as well as other impurities deposited on the foam. In a typical process, an NF piece cut in 1×1 cm^2 dimension was immersed in a 6M HCL solution and sonicated for 30 minutes. Then obtained NF was washed with DI water and ethanol several times. The cleaned NF was then dried in the vacuum oven at 60°C for 10 hours. In a separate process, 2.5mmol $Co(NO_3)_2$ and 2.5mmol Na_2MoO_4 were mixed in the 50 ml DI water and stirred for a half-hour with Teflon coated magnetic stirrer. The solution is then transferred to Teflon lined steel autoclave on which the pretreated NF was added vertically suspended in the solution. The autoclave with $CoMoO_4$ precursor and NF was then put in the oven and the temperature was maintained at 180°C for 12 hours. After the autoclave came down to room temperature the NF now coated with pink substitute was taken out and thoroughly washed with DI water to remove the obvious debris of deposited yield. To further clean the NF off large $CoMoO_4$ particles it was sonicated in DI water for few minutes. It was then washed with DI water followed by ethanol several times and kept in the oven for drying at 60°C for 10 hours. Finally, the self-grown $CoMoO_4$ on NF was obtained by annealing the dried NF at 300°C for 3 hours under argon atmosphere. The mass of the active material for several electrodes is around 3~3.5 mg/cm^2. The final product obtained was named as CMO-NF.

4.2.2. Preparation of CMO-GC

Glucose was used as a carbon precursor for treating the CMO-NF electrodes obtained from the aforementioned steps. In a typical process, 1mmole glucose was dissolved in 50ml of DI water with the help of magnetic stirrer. After the complete dissolution of glucose, the solution was transferred to the Teflon lined steel autoclave. The CMO-NF stripe was immersed vertically in the above solution and the autoclave was kept in the oven at 180°C for 12 hours. After the autoclave came down to room temperature, the CMO-NF sample covered with dark grey carbonaceous glucose debris was then washed with DI water followed by ethanol for several times. Washing was done until there were no visible solid particulates in the CMO-NF stripe. Finally, the stripe was dried in the oven at 60°C for 5 hours and then in the furnace at 600°C for 3 hours under argon atmosphere. The black NF stripe obtained at last was named as CMO-GC owed to the use of glucose as a carbon source. To understand the carbon formation process and the effect of precursor molarity in its content, different molarity of glucose was used to synthesize the CMO-GC electrodes. Typically, 1,2,3 and 4 mmol of glucose were used to treat the CMO-NF electrodes maintaining all other conditions the same. The respective samples were named as CMO-GC-1, CMO-GC-2, CMO-GC-3, and CMO-GC-4.

4.2.3. Working electrodes preparation

The as-synthesized CMO-NF and CMO-GC were used as a positive electrode without further treatments. The negative electrode was prepared by a slurry coating process where activated carbon (AC) was used as an active material. The peanut shell derived activated carbon was synthesized in our lab and already reported as a promising negative electrode in a supercapacitor device application[145]. In a typical process 85

weight % activated carbon, 10 weight % super P, and 5 weight % PVDF were mixed with the help of N-methyl pyrrolidone to form a slurry. The slurry was then coated in the pre-treated (1×1 cm^2) bare nickel foam and dried at 110°C for 10 hours in a vacuum oven.

5. RESULTS AND DISCUSSIONS

5.1. Battery

5.1.1. Physical characterization results

Obtained nanocomposites have been characterized using different approaches like XRD analysis by using the PANanalytical's Empyrean XRD with Cu Kα (λ = 0.15405 nm) radiation in the scan range (2θ) of 5° to 80°. The structural morphologies of the samples were observed with a field emission scanning electron microscope (TESCAN, MIRA3), and chemical compositions were evaluated by energy-dispersive spectroscopy (EDS) measurements and element mapping (TESCAN, MIRA) measurements at 15 kV.

In addition to the CoMoS and CoMoS@NC samples, the physical characterization of the $CoMoO_4$ sample was also done in a very detailed manner as the formation of $CoMoO_4$ nanostructure could highly affect the CoMoS and CoMoS@NC in later experimental conditions. X-ray diffraction (XRD) analysis has been done to analyze the crystalline nature of the prepared $CoMoO_4$, CoMoS, and CoMoS@NC nanocomposites. As shown in Figure 5.1(A), XRD patterns of $CoMoO_4$ are consistent and well agreed with the standard XRD pattern (JCPDS No. 21-0868). The sharpest diffraction peaks at 26.45° can be indexed as the (002) crystal planes of monoclinic $CoMoO_4$. Similarly, crystal planes associated with different 2 theta values can be observed in the figure. Overall, relatively sharp and distinct peaks can be seen depicting rather good crystallinity of $CoMoO_4$ nanoparticles. Moreover, nonappearance of extra peaks suggests the high purity of the prepared sample. Likewise, Figure 5.1(B) shows the XRD pattern of CoMoS and CoMoS@NC nanoparticles. As seen in the figure for

the CoMoS sample, no significant diffraction peaks are observed suggesting that the CoMoS compound formed is amorphous in nature. The amorphous nature of the material is believed to facilitate more transportation channels compared to good crystallinity material and hence favorable for the good electrochemical applications. On the contrary, the CoMoS@NC sample shows the diffraction peaks and perfectly matched with the $CoMoS_{3.1}$ phase (JCPDS No. 16-0439). The alkaline environment during dopamine treatment and repeated annealing process may be the reason for its crystalline nature. In addition to the $CoMoS_{3.1}$ peaks, the appearance of carbon peak around 26.5 2Theta degree corresponds to the 002 lattice plane and clearly shows the presence of carbon in the compound.

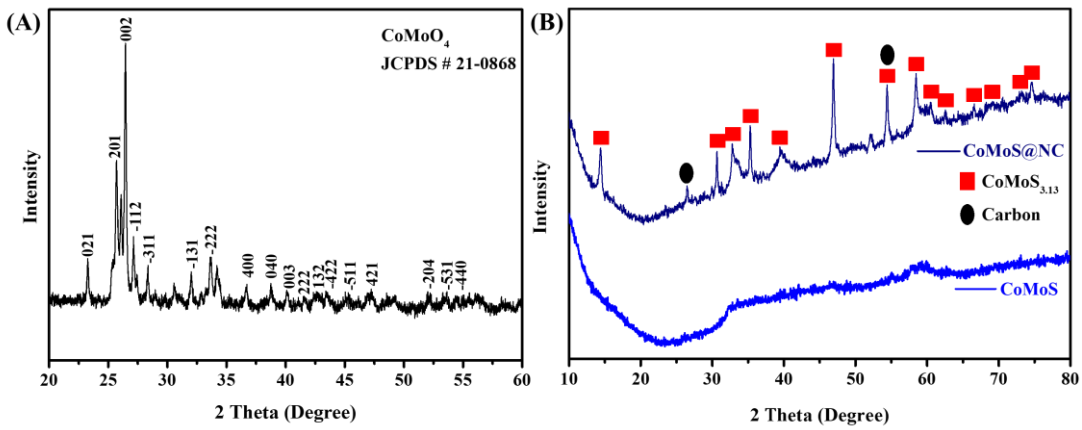

Figure 5.1 XRD-spectrum of $CoMoO_4$ (A) and CoMoS & CoMoS@NC nanocomposites (B).

FE-SEM images of as-prepared samples can be seen in Figure 5.2. Figure 5.2 A1 shows the overall appearance of the pristine $CoMoO_4$ sample. Several nano-sized rod-like structures are formed. Closer magnification in Figure 5.2 A2 shows the uniformity in those structures. The average dimension of each nanorod is measured to be around 30 nm in diameter and 200 nm in length. Furthermore, numerous needles like structures can be seen protruding from the surface of each nanorod.

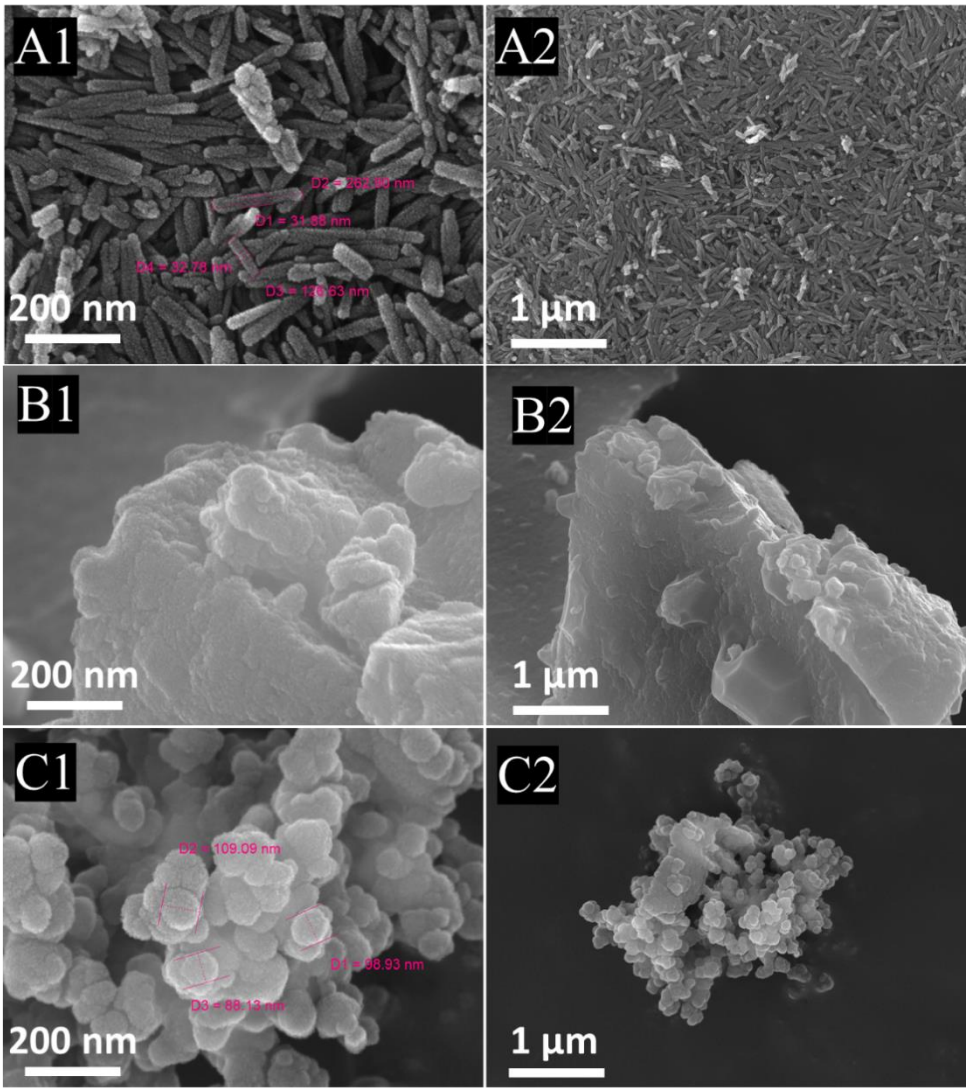

Figure 5.2 SEM image of $CoMoO_4$ (A) CoMoS (B) and CoMoS@NC (C).

Figures 5.2 B1 and B2 represent the FE-SEM image of the CoMoS sample under 200 nm and 1 µm resolution respectively. Overall observation shows a radical change in appearance and dimension from $CoMoO_4$ rod-like structures. No definite physical structure can be observed. Instead, the aggregated solid amorphous mass was formed. The amorphous nature of the CoMoS was also supported by the XRD analysis. Figures 5.2 C1 and C2 represent the SEM image of CoMoS@NC under 200 nm and 1 µm resolution respectively. The formation of spherical structures can be seen under high resolution. The size of the nanospheres formed is measured to be around 90 nm. Alkali

environment during the dopamine treatment as well as the presence of polydopamine around the CoMoS is believed to be the cause of change in the surface morphology.

EDS elemental mapping was also done to verify the composition of elements present in $CoMoO_4$, CoMoS, and CoMoS@NC. Elemental mapping images in Figure 5.3 shows the uniform distribution of Co, Mo, and O elements in the $CoMoO_4$ nanocomposite. The element molar ratio of Co, Mo, and O is about 1:1:4, which is corresponding to the composition of $CoMoO_4$.

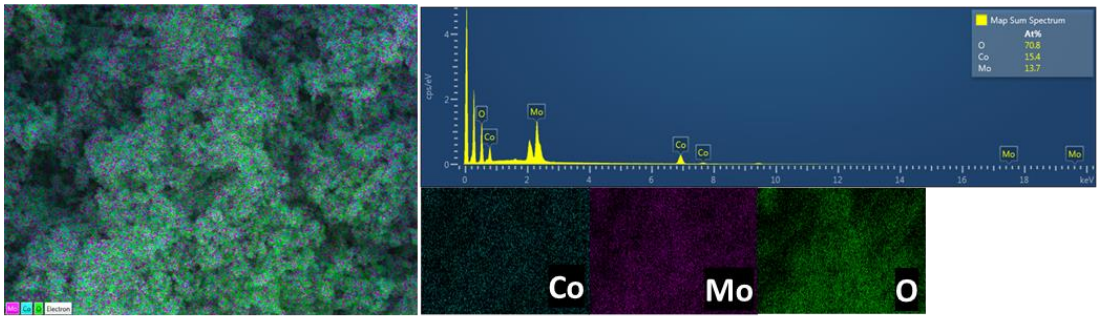

Figure 5.3 EDS elemental mapping image of $CoMoO_4$.

Figure 5.4 shows the EDS image of the CoMoS sample. The presence of Co, Mo, and S is well revealed, and the atomic weight percentage is in agreement with $CoMoS_{3.1}$ Shown by the XRD in the CoMoS@NC sample. Likewise, the EDS image of CoMoS@NC is shown in Figure 5.5. Besides the anticipated Co, Mo, and S elements, a carbon presence of almost 60 atomic weight percentage supports the carbon peaks shown in the XRD spectrum.

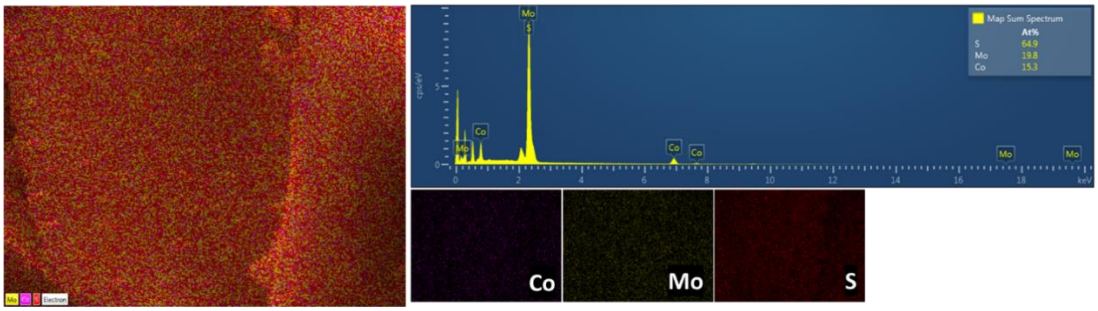

Figure 5.4 EDS elemental mapping image of CoMoS nanocomposite.

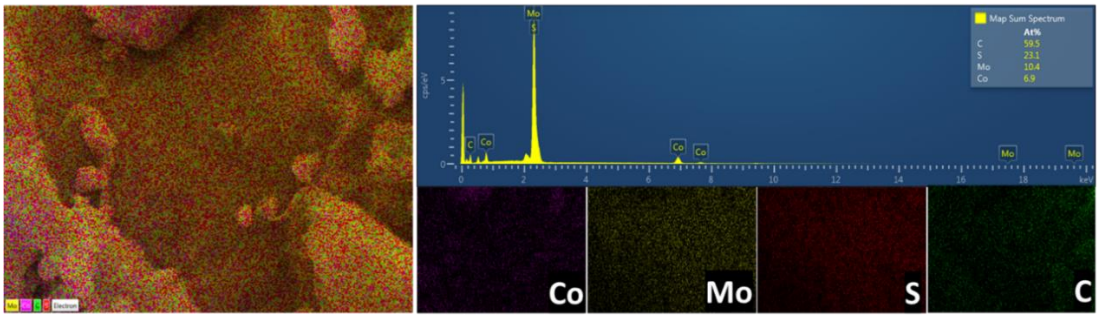

Figure 5.5 EDS elemental mapping image of CoMoS@NC nanocomposite.

5.1.2. Electrochemical characterization results

The working electrodes were prepared by using a slurry-coating procedure [146, 147]. The slurry was prepared by mixing 70 wt.% active material (CoMoS and CoMoS@NC), 15 wt.% carbon black, and 15 wt.% CMC binder using DI water as a solvent. The mixture was hand-ground with mortar and pistol until there were no granular particles remained. Then the slurry was casted onto a copper foil and dried at 110 °C for 10 h under vacuum. Thus, prepared copper foil coated with active material was clamped with 12mm dia. crimper for an electrode. Test cells (CR 2032) were assembled in an argon-filled glove box with a metallic lithium foil as a reference electrode, 1M $LiPF_6$ electrolyte dissolved in ethylene carbonate/dimethyl carbonate (EC: DMC=1:1 v/v), and a Celgard 2400 polypropylene (PP) microporous film as a separator. Galvanostatic charge/discharge tests were conducted on PESC05-0.1 PNE

Power and Energy Solution cell cycler in the voltage range of 0.001–3.0 V at a controlled room temperature of 25°C.

Several numbers of CR-2032 half coin cells with CoMoS and CoMoS@NC as an active material were assembled inside the glove box. All cells were checked for a satisfying value of open-circuit voltage (OCV). The capacity of the composites in the current study is based on the mass of active material. Several charge-discharge cycles were run for each cell at a constant current density of 200mA/g. Charge-discharge cycles at different current densities from 100mA/g to 1000 mA/g were performed as a stability test. Before all, electrochemical impedance spectroscopy was performed to check for the charge transfer resistance of the as-fabricated half cells. As we can see in Figure 5.6 both CoMoS and CoMoS@NC electrodes exhibit the semicircle structure in the high-frequency region and straight line in the low-frequency region. The semicircle represents the charge transfer resistance (R_{ct}) of the interface between the electrode and electrolyte [148]. The linear line in the lower frequency region represents the Warburg impedance and corresponds to the diffusion of ions into the pores of the electrode material [149]. The equivalent series resistance (R_s) corresponds to the combined resistance of active material, ionic resistance of the electrolyte, and active material/current collector interface [150]. Respective values for the equivalent electrical component can be seen in table 5.1.

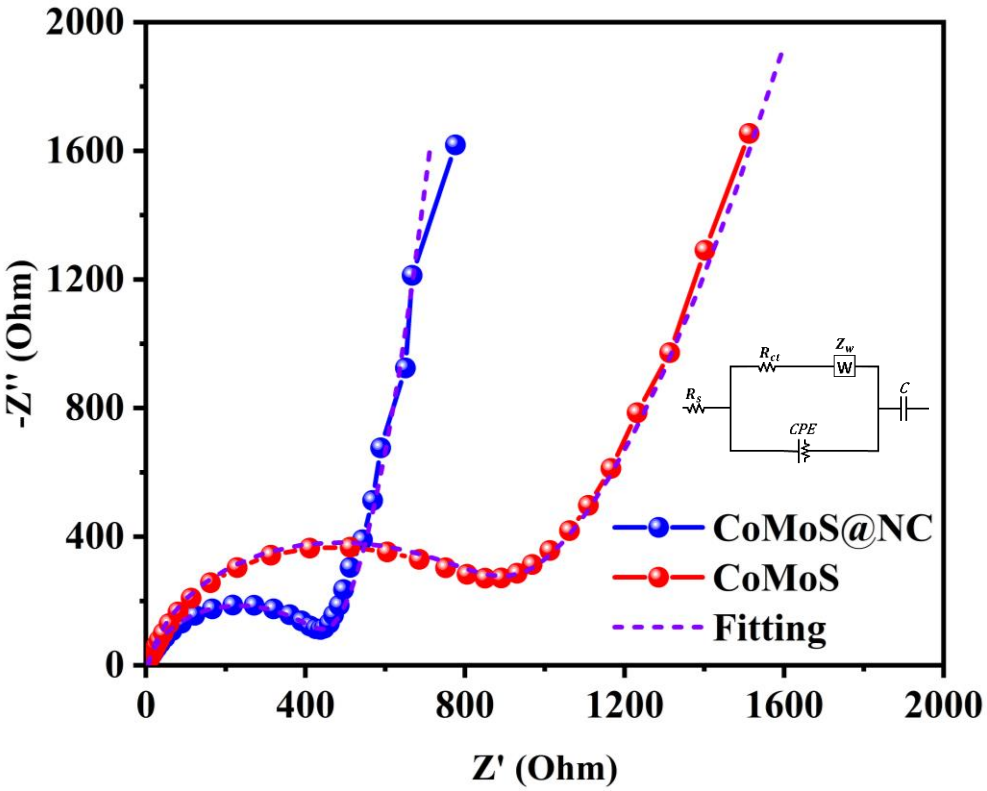

Figure 5.6 EIS of CoMoS@NC and CoMoS half cells.

Table 5.1 EIS equivalent electrical component values for CoMoS and CoMoS@NC half cells.

	R_s	R_{ct}	Z_w	CPE	C
CoMoS	6.2Ohm	850.0 Ohm	1 mMho	7.2 µMho	1.0 mF
CoMoS@NC	4.1 Ohm	430.0 Ohm	10 mMho	88.5 mMho	12.0 mF

As seen in Table 5.1 the charge transfer resistance (R_{ct}) and the equivalent series resistance (R_s) both are significantly dropped for the CoMoS@NC half-cell. The improved charge transferability is attributed to the presence of a nitrogen-doped carbon matrix over the CoMoS composite that facilitates the improved ions mobility and hence superior electrical conductivity.

Figure 5.7(A) shows the charge-discharge profile of the CoMoS half-cell at 200 mA/g current density between the potential range of 0.01–3 V for the 1st, 2nd, 10th, 20th, 30th, 40th, 50th, 60th, 80th, and 100th cycles. Figure 5.7(B) shows the charge-discharge capacities of the same cell in terms of coulombic efficiency.

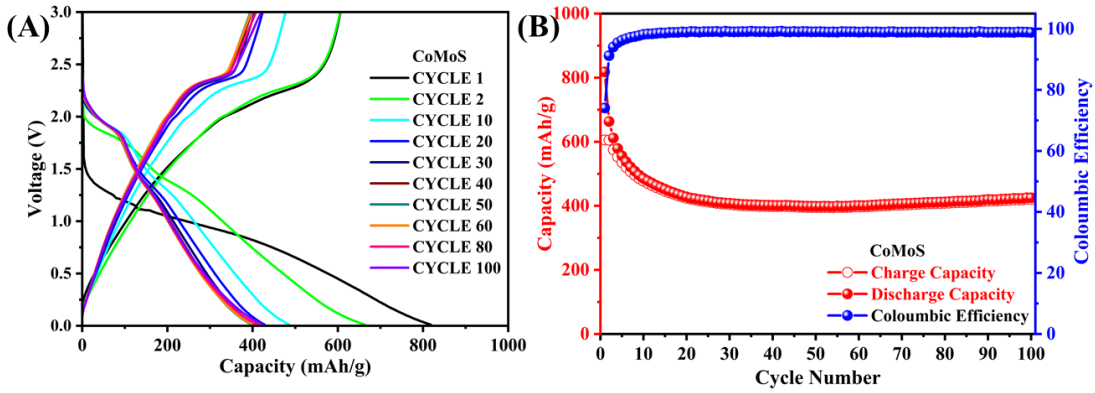

Figure 5.7 Cyclic performance (A) and charge-discharge capacities with coulombic efficiency (B) of CoMoS half-cell.

As seen in the figure, the first discharge and charge capacity for CoMoS cell is registered as 818 mAh/g and 605.88 mAh/g respectively. Whereas for the second cycle the discharge and charge capacities are 664.45 mAh/g and 605.18 mAh/g. The coulombic efficiency for the first and second cycles is 74 % and 91% respectively. The irreversible capacity loss in the 1st and 2nd cycles is attributed to the formation of a solid electrolyte interface (SEI) layer [8, 151, 152]. The charge-discharge capacities from the 3rd cycle onward are almost similar and registered a coulombic efficiency of almost 100 percent up to the 100th cycle. Also, after constant capacity fading up to around the 25th cycle, the charge-discharge capacities remained unchanged until the 100th cycle. The discharge and charge capacity at 100th cycles are 425.22 mAh/g and 420.23 mAh/g respectively.

The charge-discharge profile of the CoMoS@NC cell can be seen in Figure 5.8(A) Great improvement in the charge-discharge capacities can be seen compared to that of the CoMoS cell. Discharge and charge capacity for the 1st, 2nd, and 3rd cycles are 1010.25 mAh/g and 818.21 mAh/g, 924.22 mAh/g, and 866 mAh/g, 788.73 mAh/g and 777.43 mAh/g respectively. The coulombic efficiency is 81%, 93.74%, and, 98.5% for the respective cycles. Besides the obvious increase in the specific capacity, the CoMoS@NC cell presented some improved figures such as the substantially increased coulombic efficiency in the 1st and 2nd cycles. Higher coulombic efficiency in the starting cycles suggests the lesser material loss on the SEI layer and higher will be the specific capacity in subsequent cycles.

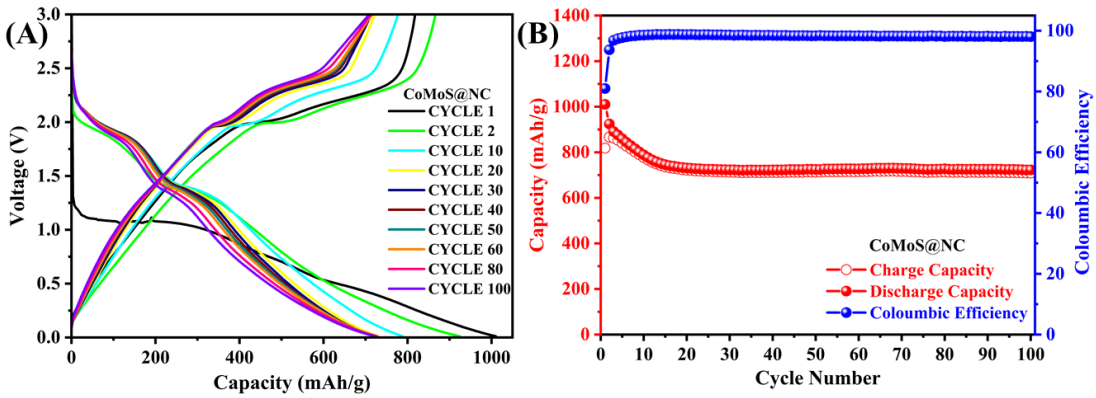

Figure 5.8 Cyclic performance (A) and charge-discharge capacities with coulombic efficiency (B) of CoMoS@NC half-cell.

Figure 5.8(B) shows the coulombic efficiency regarding the charge-discharge capacities of CoMoS@NC cells for 100 cycles. From this figure, we can more clearly see the improved performance of the CoMoS@NC cell. The capacity fading stopes even before the 20th cycles and remained unchanged until the 100th cycle. The discharge and charge capacity of the 100th cycles are 723.12 mAh/g and 709.06 mAh/g respectively which is almost the same as that of the 20th cycle. The regularity and

absence of any sudden change in the specific capacity suggest the excellent reversible cyclability of both cells. However, CoMoS@NC kept the reversibility with even higher specific capacities at the same current density. Excellent cyclic performance for CoMoS@NC is attributed to the presence of a nitrogen-doped carbon matrix around the CoMoS composite. Carbon encapsulation of pristine CoMoS increases the charge transfer conductivity and also provides a buffer for repetitive volume expansion and compression during the lithiation and de-lithiation process respectively[153].

Figure 5.9 shows the specific capacities of CoMoS and CoMoS@NC coin cell with different current densities ranging from 100mA/g to 1000mA/g, and back to 100mA/g. For the CoMoS cell, the discharge capacity registered at the end of each current density cycle is 569.51 mAh/g, 484.07 mAh/g, 382.33 mAh/g, 305.68 mAh/g, 248.06 mAh/g, 197.77 mAh/g and back to 572.14 mAh/g. Despite the smaller specific capacity, the CoMoS cell also performed well under different current densities and retained its original value at the end.

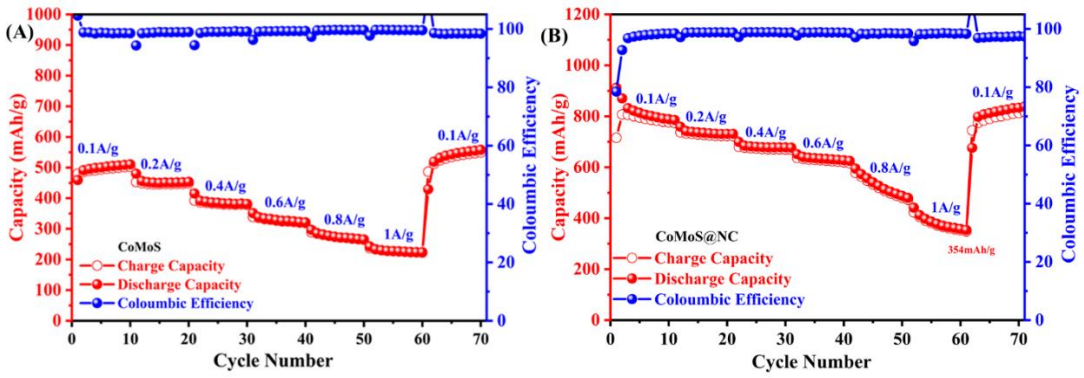

Figure 5.9 Coulombic efficiency and the Cyclic performance of CoMoS (A) and CoMoS@NC (B) under a different current density.

On the other hand, as we can see in the Figure 5.9(B), the CoMoS@NC cell kept its high specific capacity throughout the different current densities. The respective

specific capacity registered at the end of each current density cycle are, 788.62 mAh/g, 731.32 mAh/g, 678.13 mAh/g, 627.66 mAh/g, 488 mAh/g, 354.15 mAh/g, 838.49 mAh/g. The specific capacity for CoMoS@NC at the end of each current density cycle is almost twice with that of the CoMoS cell. The specific capacity of 354.15 mAh/g at the current density as high as 1 A/g makes the CoMoS@NC an attractive anode battery material. Also, the way it retained its capacity when the current density was reversed back to 1A/g, without any loss in the capacity shows the excellent capacity retention ability and reversibility of the cell.

5.2. Supercapacitor

5.2.1. Physical characterization results

Physical characterization of the samples was performed using different approaches like XRD analysis, FE-SEM, EDS elemental mapping. The structural morphologies of the samples were observed with a field emission scanning electron microscope (TESCAN, MIRA3), and chemical compositions were evaluated by energy-dispersive spectroscopy (EDS) measurements and element mapping (TESCAN, MIRA) measurements at 15 kV. X-ray diffraction (XRD) analysis was performed by using the PANanalytical's Empyrean XRD with Cu Kα (λ = 0.15405 nm) radiation in the scan range (2θ) of 5° to 80°**.** X-ray photoelectron spectroscopy (XPS) was conducted using a Theta Probe AR-XPS system (Thermo Fisher Scientific, U.K.) with monochromatic Al Kα at a wavelength of 1486.6 eV at 15 kV.

Figure 5.10(A) shows the XRD patterns of pristine CMO-NF and CMO-GC-2 compounds. The formation of alpha $CoMoO_4$ on the nickel foam was observed under the hydrothermal reaction, but beta $CoMoO_4$ exists after treated at high temperature.[154] The observed peaks of pristine CMO-NF are 33.6°, 59.2°, and 62.7°, which corresponds to the planes (−222), (024), and (−443) respectively. The new observed peaks of CMO-GC at 22.1°, 25.3°, 26.5°, 37.05°, and 43° are corresponding to the planes (021), (201), (002), (400), and (-422) respectively, which attributed to the beta phase of $CoMoO_4$. The peak at 26.5° is attributed to the graphitic carbon peak, which overlaps with the crystalline peak of $CoMoO_4$. The remaining peaks at 44.5°, 51.8°, and 76.4° are corresponding to the nickel foam. All the diffraction peaks are in good agreement with the previous literature and standard pattern for $CoMoO_4$ (JCPDS

No. 21–0868).[121], [155], [156] Moreover, the absence of extra peaks suggests the high purity of the prepared sample.

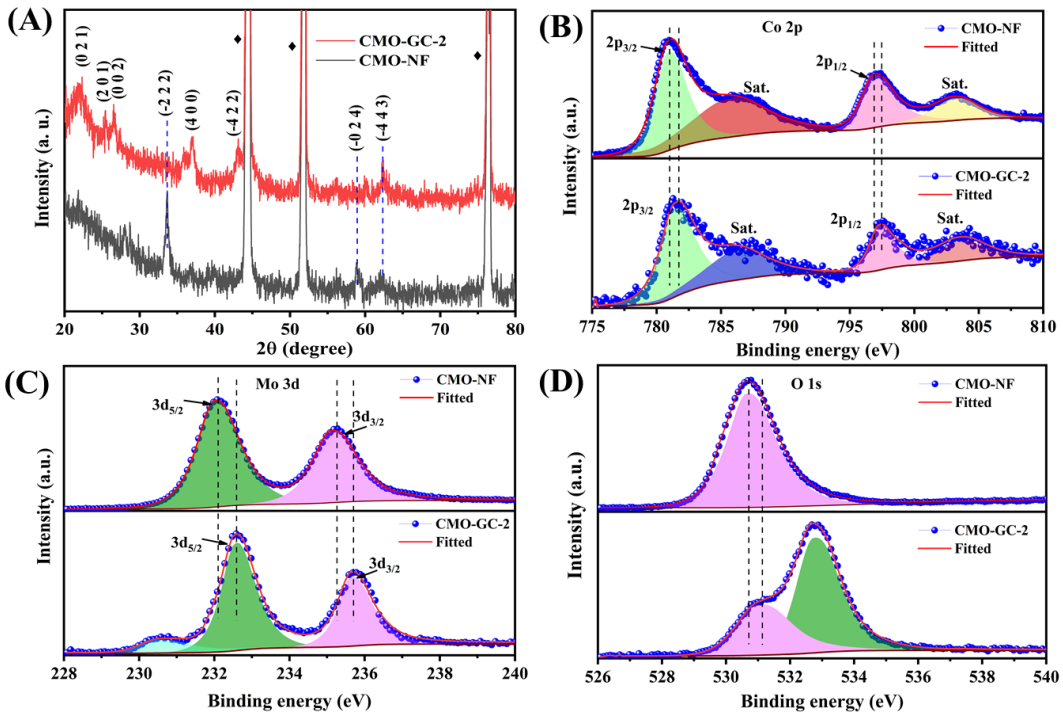

Figure 5.10 XRD pattern of CMO-NF and CMO-GC-2 (A), XPS core level spectrum of Co 2p (B), Mo 3d (C), and O 1s (D) of CMO-NF and CMO-GC-2.

The chemical states of elements on the surface of CMO-NF and CMO-GC-2 are further analyzed by XPS, shown in Figure 5.10(B-D). In the Co 2p core-level spectrum of the pristine CMO-NF, two peaks corresponding to Co $2p_{3/2}$ and $2p_{1/2}$ of Co^{2+} are observed at 780.6 and 796.8 eV, respectively[157] (Figure 5.10(B)). And two peaks associated with the $3d_{3/2}$ and $3d_{5/2}$ of Mo^{6+} are observed at 232.0 and 235.1 eV (Figure 5.10(C)), respectively.[158] The corresponding satellite peaks observed at 285.5 eV and 803.1 eV of CMO-NF are associated with the Co 2p. The Co 2p and Mo 3d profiles of CMO-GC-2 observed the four distinct peaks at a higher binding energy level at 781.4 eV and 797.3 eV associated with Co $2p_{3/2}$ and $2p_{1/2}$ of Co^{2+}, and 232.6 eV, and 235.6 eV associated with Mo $3d_{5/2}$ and $3d_{3/2}$ of Mo^{6+}, respectively.[159] The characteristic

peaks of Co^{2+} and Mo^{6+} in CMO-GC-2 shift toward higher binding energy in comparison with those of CMO-NF, suggesting the decreased density of electron cloud above CMO nanosheets after covered with carbon layers and nanospheres. The electron transfer from CMO to carbon indicates strong coupling between CMO and carbon coating. In Figure 5.10(D), the XPS core level spectrum of O 1s of CMO-NF shows low binding energy level at 530.7 eV is attributed to the O^{2-} forming oxide with cobalt and molybdenum. In the case of CMO-GC-2, the two centric peaks of O 1s observed at 531.1 eV and 532.8 eV are attributed to the O^{2-} state of species, and the higher energy level at 532.8 eV is attributed to the O^{2-} forming the hydroxyl group from the carbon compound.[160].

The XPS core level spectrum of C 1s of the all-carbon grown electrodes is shown in Figure 5.11. The deconvolution peaks of the C 1s spectrum are also resolved into three components, centered at 284.6 eV(C1), 285.5 eV(C2), 288.0 ± 0.3 eV(C3) that are attributed to the existence of graphite carbon (C-C), hydroxy (C-O) and keto groups (C=O), respectively [161].

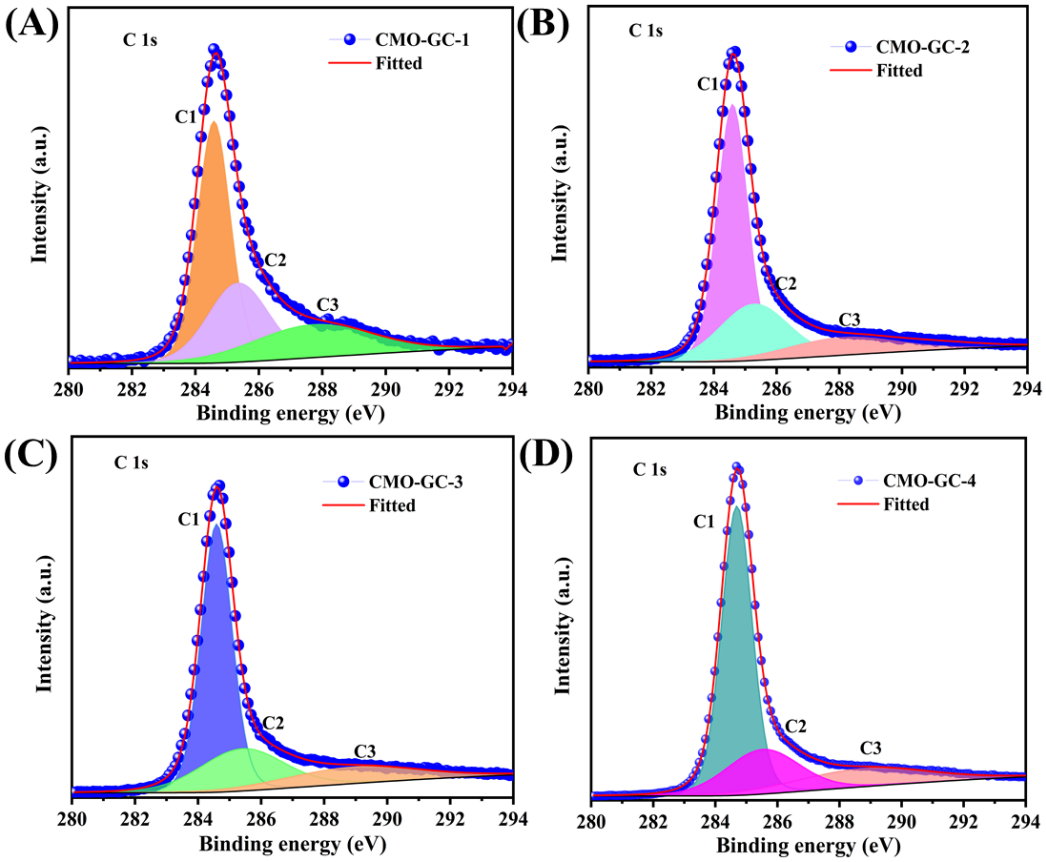

Figure 5.11 XPS core level profile of C 1s of the CMO-GC-1 (A), CMO-GC-2 (B), CMO-GC-3 (A), and CMO-GC-4 (D).

FE-SEM images of as-prepared CMO-NF samples can be seen in Figure 5.12. The general morphology of the $CoMoO_4$ nanoparticles grown on the Ni substrate can be seen on 50 µm magnification. Closer magnification at 500 nm shows the arrays of homogenously grown 3-D nanoplate structures. The average thickness of each nanoplate is measured to be around 90 nm.

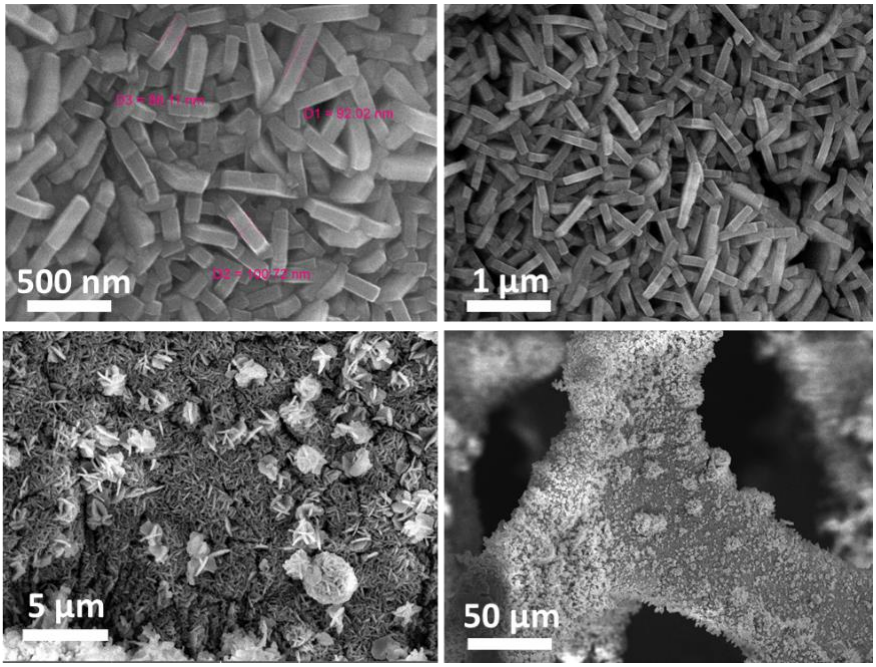

Figure 5.12 FE-SEM image of CMO-NF.

Elemental mapping images of the same sample in Figure 5.13 shows the uniform distribution of Co, Mo, and O elements in the CMO-NF electrode. The element molar ratio of Co, Mo, and O is about 1:1:4, which is corresponding to the composition of $CoMoO_4$.

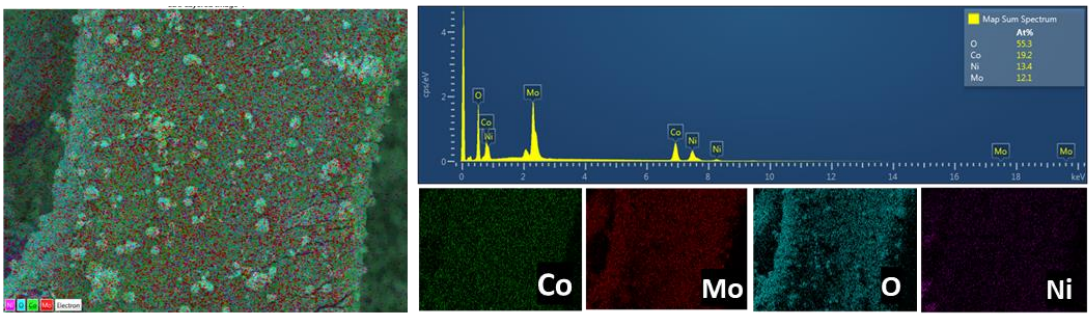

Figure 5.13 EDS elemental mapping image of CMO-NF.

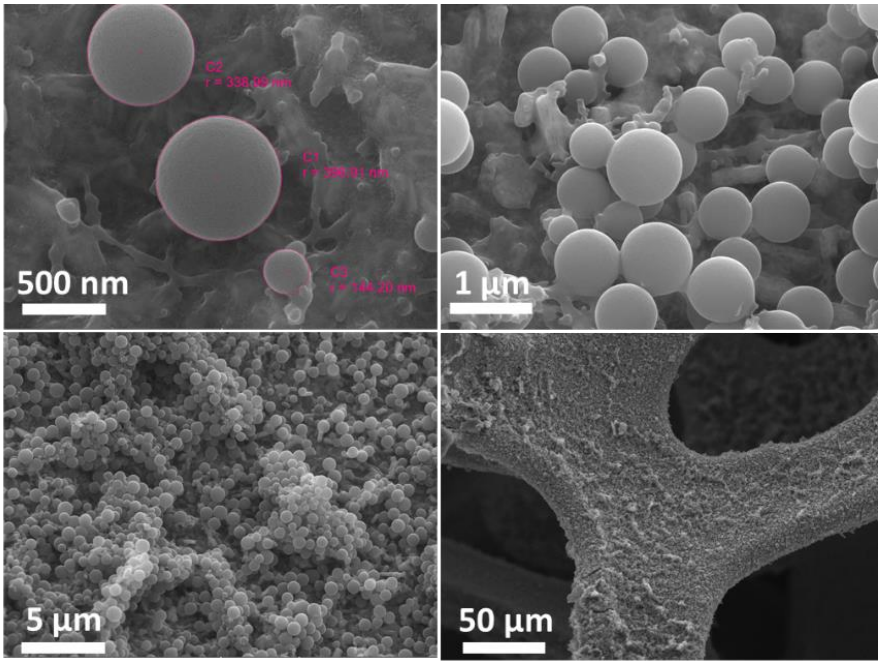

Figure 5.14 FE-SEM image of CMO-GC-2.

Figure 5.14 represents the FE-SEM image of the CMO-GC-2 sample, prepared with a 2mmol glucose precursor. Overall observation in lower magnification at 50 µm shows a substantial change in appearance compared to that of the CMO-NF. The $CoMoO_4$ nanoplates are completely glazed by the thin film deposition and numerous nanospheres are formed over the thin film. The nanospheres formed are believed to be the carbon nanospheres which are uniformly distributed with an average radius of 300 nm. The higher magnification at 500 nm and 1 µm show the uniformity and smoothness in the carbon nanospheres. The nanospheres are believed to provide an excellent specific capacity and energy density when fabricated to a supercapacitor device. Mainly because of their shape that provides an additional surface area to hold the ions around them.

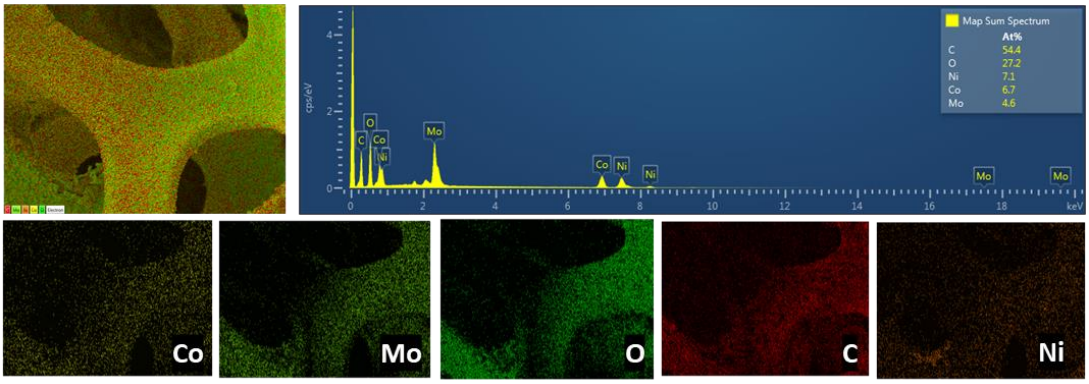

Figure 5.15 EDS elemental mapping image of CMO-GC-2.

The EDS image of the CMO-GC-2 sample in Figure 5.15 well revealed the presence of Co, Mo, O, and C elements. Also, the elemental weight ratio provides a good perception of the composition of the materials present. In addition to the anticipated atomic weight ratio of Co, Mo, and O, the existence of 54% Carbon validates the presence of a homogenously dispersed carbon matrix on the surface of the electrode. The large presence of carbon thin film and nanosphere matrix is believed to facilitate the charge transferability of the electrode as well as provide the physical support for the $CoMoO_4$ carbon nanoplates during the continuous charge-discharge process.

The samples prepared with different molarity of glucose were also analyzed with SEM and EDS analysis. Figure 5.16 shows the SEM image of CMO-GC-1. As we can see the 1mmol glucose precursor did not yield any nanospheres on the substrate surface. Even after careful examination of several spots on the sample, no carbon nanospheres were observed. Rather, a thin layer of coating on top of the CMO nanoplates is observed and the structural morphology of the $CoMoO_4$ nanoplates is still noticeable. Also, the reduced atomic weight percentage of carbon species is observed from EDS analysis.

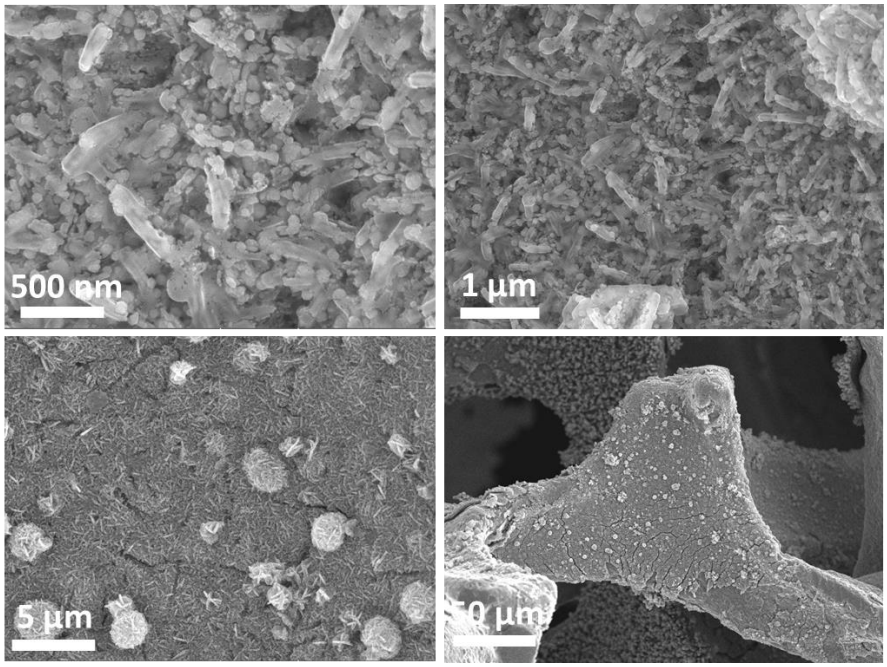

Figure 5.16 FE-SEM image of CMO-GC-1.

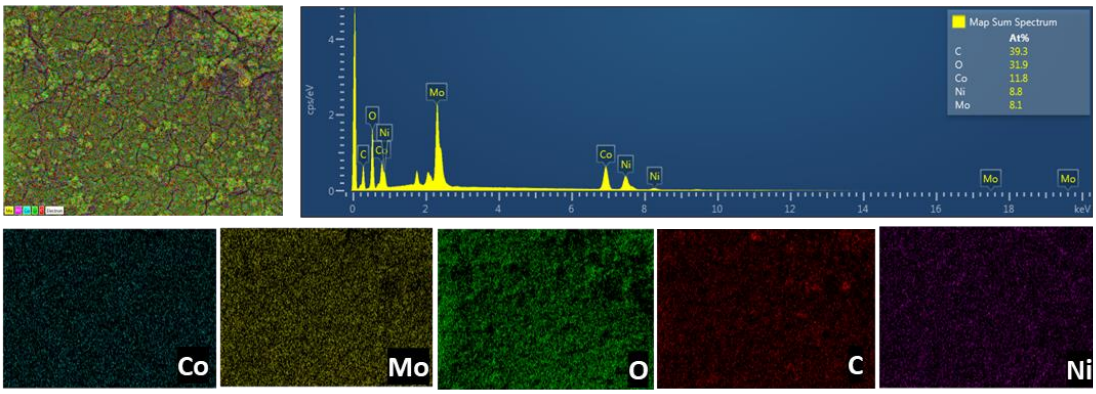

Figure 5.17 EDS elemental mapping of CMO-GC-1.

The surface morphology of the CMO-GC-3 sample can be seen in Figure 5.18. Unlike the CMO-GC-1 sample, the $CoMoO_4$ nanoplates structure is not observable in this case. Furthermore, means a good amount of carbon film coating can be assumed to dissipate over the $CoMoO_4$ nanostructure

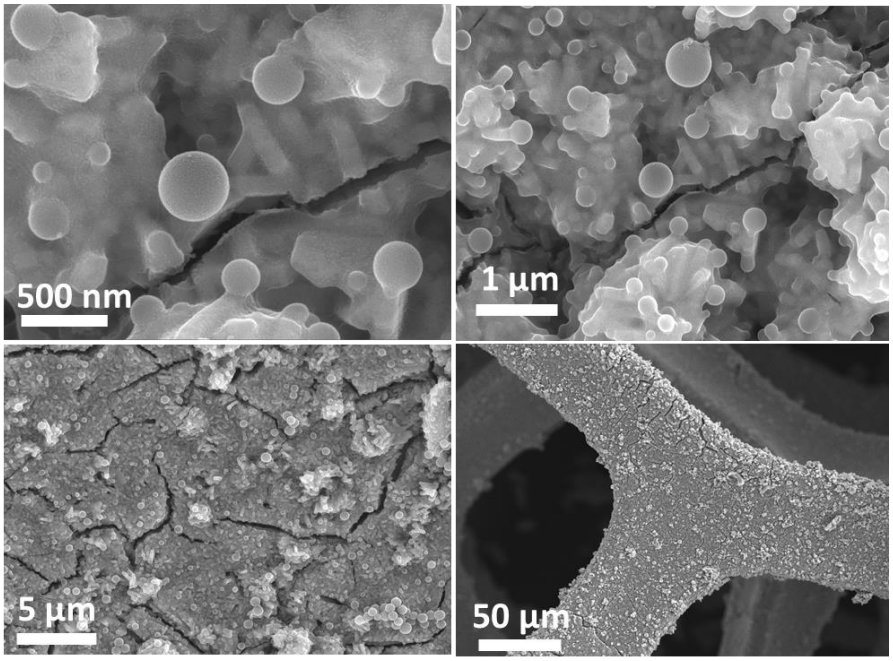

Figure 5.18 FE-SEM image of CMO-GC-3.

In addition to the thin film, very few carbon nanospheres were observed in comparison to the CMO-GC-2 sample. Also, few nano cracks were spotted which might compromise the adhesion of the CMO-GC-3 with the Ni substrate and hinder the stability of the supercapacitor device in the long run. In Figure 5.19 EDS mapping of the sample shows the expected atomic weight percentage of respective elements. However, the amount of carbon is still lower than that of CMO-GC-2. A decreased number of carbon nanospheres could be the reason for lower carbon yield.

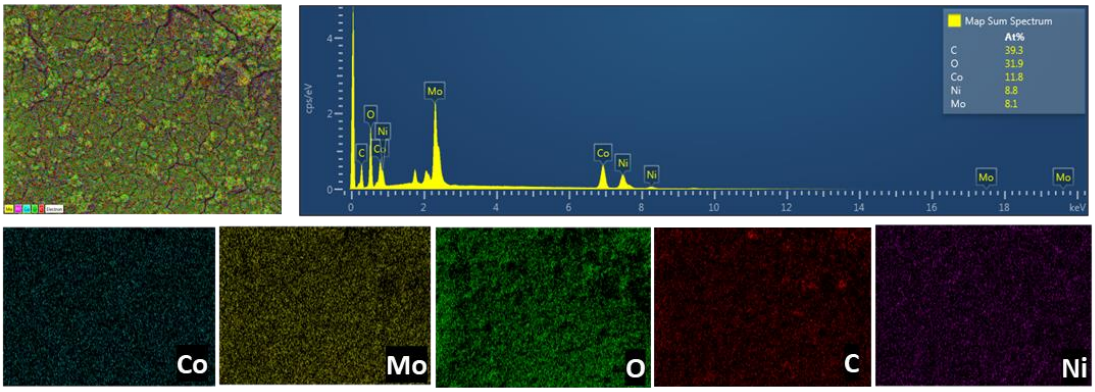

Figure 5.19 EDS elemental mapping of CMO-GC-3.

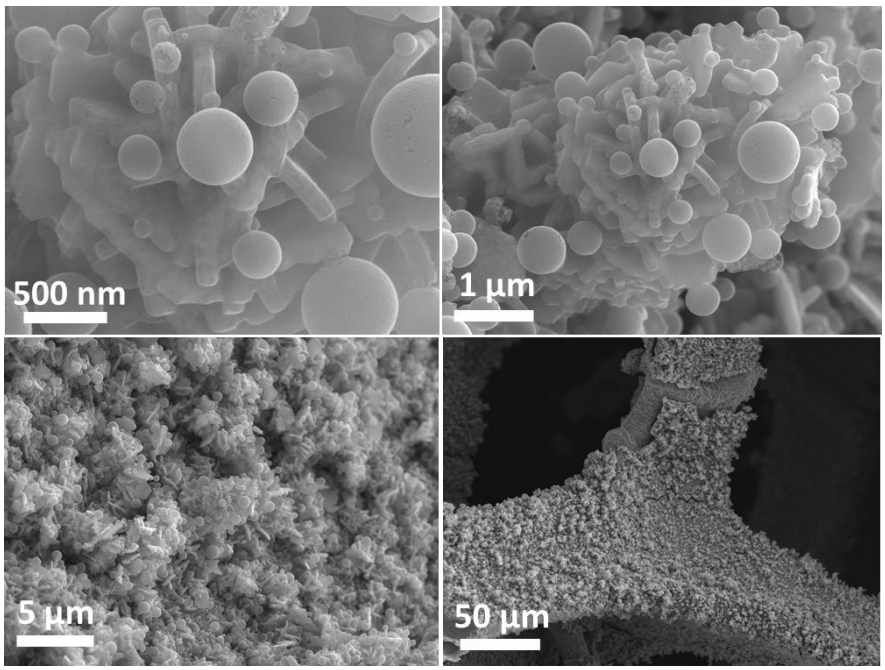

Figure 5.20 FE-SEM image of CMO-GC-4.

Figure 5.20 shows the SEM image of the CMO-GC-4 sample. Here we can observe the increased number of carbon nanospheres as compared to CMO-GC-3 sample. However, almost all the nanospheres seem to be suffered from surface defects. Instead of a smooth surface, the nanosphere's appearance is teared up and cracked. We can assume the defect in the nanosphere may limit the performance of the CMO-GC-4 electrode.

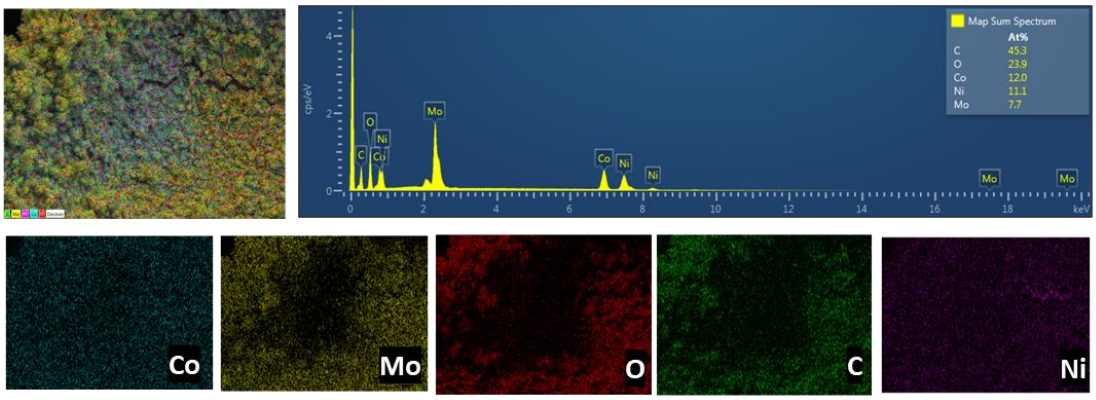

Figure 5.21 EDS elemental mapping of CMO-GC-4.

The EDS mapping of the same sample shows the increased carbon content which supports the obvious reasoning that increasing the glucose amount increases the carbon yield. On the contrary, the maximum carbon yield was with the 2mmol glucose, which we believe is the optimal concentration of glucose to produce the perfectly shaped maximum amount of carbon. The remaining elemental composition is per their theoretical values.

5.2.2. Electrochemical characterization results

The electrochemical measurements were carried out using an AUTOLAB PGSTAT204N electrochemical workstation in which Cyclic Voltammetry (CV), Galvanostatic Charge Discharge (GCD), and Electrochemical Impedance Spectroscopy (EIS) were performed. Three electrode system was employed for the electrochemical measurements where CMO-NF and CMO-GC were the working electrodes for their respective analysis. Platinum foil (0.8 × 0.8 cm^2) was used as a counter electrode and silver/silver chloride (Ag/AgCl) was used as a reference electrode. Whereas 2.0 M KOH solution was used as an electrolyte solution. CV tests were carried out in the potential window of -0.1 V to +0.55 V at the sweep rates of 5-150 mV/s for the CMO-NF as well as CMO-GC electrode and -1 V to 0 V for the negative electrode. GCD tests

were carried out between the potential window of -0.1 V to 0.42 V for positive electrodes and -1 V to 0 V for negative electrodes at various current densities. EIS was carried out in the frequency range from 100 kHz to 0.01 Hz.

Figure 5.22 (A) shows a CV plot of the CMO-NF electrode at scan rates from 5mV/s to 150mV/s between the potential range of -0.1V to +0.55V vs. standard Ag/AgCl electrode. Figure 5.22 (B) on the right shows the CV plot of CMO-NF electrode and a bare nickel foam electrode at 5 mV/s, depicting the capacitive share of nickel substrate on further electrochemical measurements will be negligible.

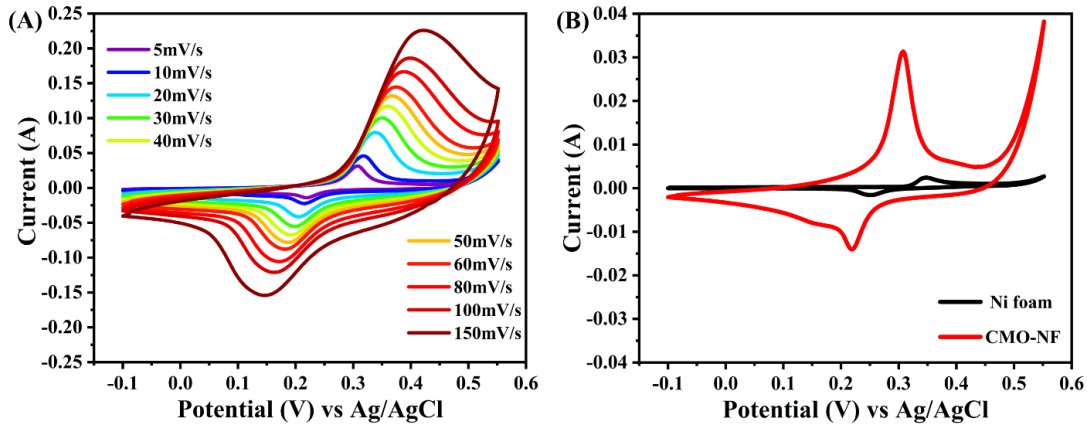

Figure 5.22 CV of CMO-NF (A) and CV comparison of CMO-NF and NF (B).

Contrary to the EDLCs which offer almost rectangular CV plots, the CV plot of CMO-NF shows rather proportioned strong redox peaks corresponding to the respective anodic and cathodic sweeps, which suggests the specific capacitance is mainly governed by the Faradic reactions. While observing a single CV plot of CMO-NF at 5mV/s, the anodic peak at around 0.32 V and cathodic peaks at around 0.22 V can be seen. The respective peaks are the outcomes of oxidation and its reverse process. The faradic redox reactions that are taking place on corresponding scans can be summarized as follows[122][162]:

$$3(Co(OH)_3)^- \leftrightarrow Co_3O_4 + 4H_2O + OH^- + 2e^- \quad \text{.....(9)}$$

$$Co_3O_4 + H_2O + OH^- \leftrightarrow 3CoOOH + e^- \quad \text{.....(10)}$$

$$CoOOH + OH^- \leftrightarrow CoO_2 + H_2O + e^- \quad \text{.....(11)}$$

Furthermore, the linear increment of anodic and cathodic peak currents with the scan rates and the way CV curves maintained their shapes throughout the increment shows the rapid ionic and electronic movements, good electronic conductivity, and electrochemical reversibility even in the high scan rates.

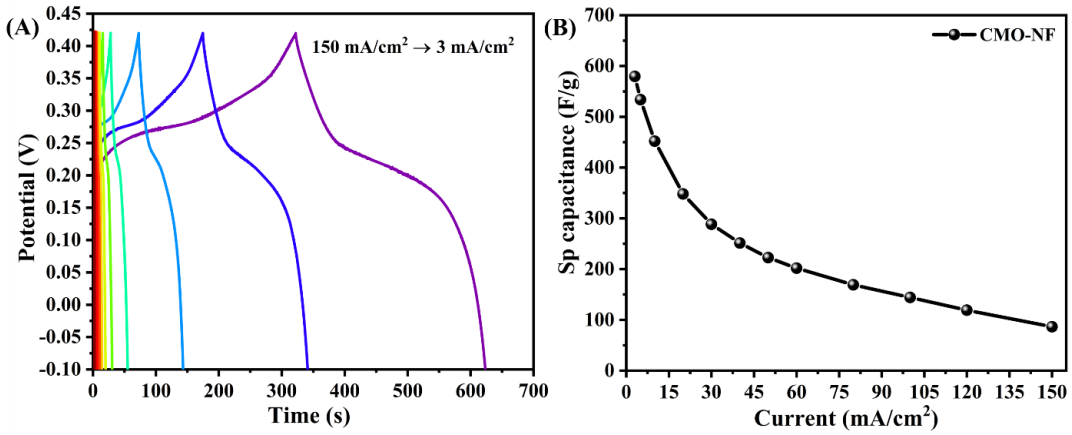

Figure 5.23 GCD plot of CMO-NF (A) and Specific capacitance of the same electrode (B).

Figure 5.23 (A) shows the galvanostatic charge-discharge cycles of the CMO-NF electrode between the voltage range of -0.1 V to 0.42 V from current densities of 3mA/cm^2 to 180mA/cm^2. The nonlinear nature of GCD curves supports the pseudocapacitive nature of the active material and is also consistent with the CV results demonstrated earlier. The specific capacitance was calculated from the data obtained from the GCD cycles using the following formula,

$$C_s = \frac{i \times \Delta t}{m \times \Delta V} \quad \text{.....(12)}$$

Where i is the applied current, Δt is the discharge time, m is the mass of the active material, and ΔV is the potential window.

Figure 5.23(B) shows the specific capacitance of the CMO-NF electrode relating to different current values. The specific capacitance of 580 F/g is obtained for the 1A/g current density (3mA/cm^2). The obvious capacitance fading in forthcoming current values is attributed to the insufficient active material participation in redox reaction at high current density.

Figure 5.24(A) shows the CV plots of CMO-GC-2 electrode at different scan rates in the potential window of -0.1 V to 0.55 V. The area of the CV curve is notably increased for the glucose treated electrode compared to the pristine CMO-NF electrode. For a stark observation, the comparative CV plots of CMO-NF and CMO-GC-2 electrode is plotted, which can be seen in Figure 5.24(B)

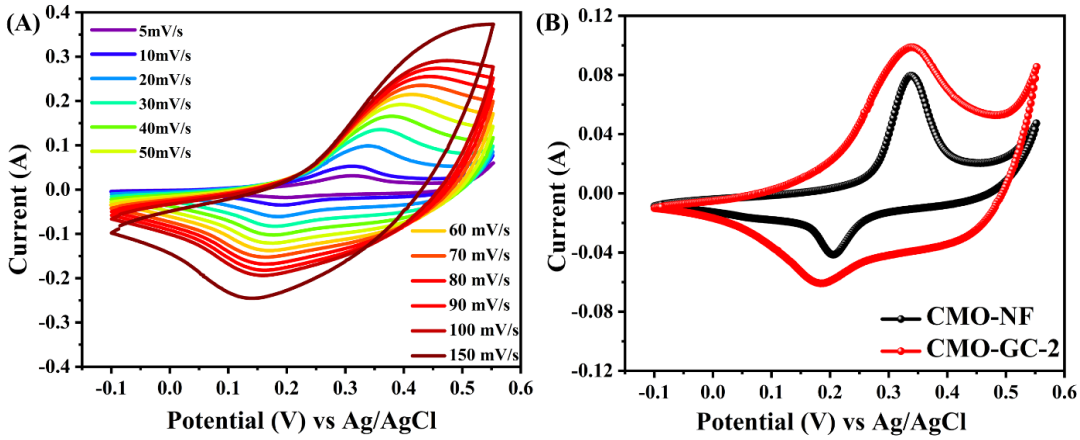

Figure 5.24 CV of CMO-GC-2 (A) and CV comparison of CMO-GC-2 and CMO-NF (B).

The increased area is facilitated by the presence of carbon nanospheres and nanolayers matrix, which improves the ionic movement along with the electrochemical conductivity of the electrode.

Figure 5.25(A) shows the GCD plots of CMO-GC-2 electrode done within the potential range of -0.1 V to 0.42 V for the input current ranging from around 1 mA/cm^2 to 150 mA/cm^2. The charge-discharge profile of glucose treated electrode covers a much higher area compared to an untreated CMO-NF electrode.

The GCD plot comparing the charge-discharge nature of both electrodes can be seen in Figure 5.25(B) at the current density of 1 A/g. The vast increase in charge-discharge time in the case of CMO-GC-2electrode is attributed to the incorporation of a carbon nano matrix. The carbon incorporation provides aid on the ion intercalation-deintercalation mechanism by effectively increasing the contact area between the active material and the electrolyte. Furthermore, it also increases the overall electrical conductivity of the electrode. Using equation 4, the specific capacitance for CMO-NF and CMO-GC-2 has been calculated and the comparative plot can be seen in Figure 5.26.

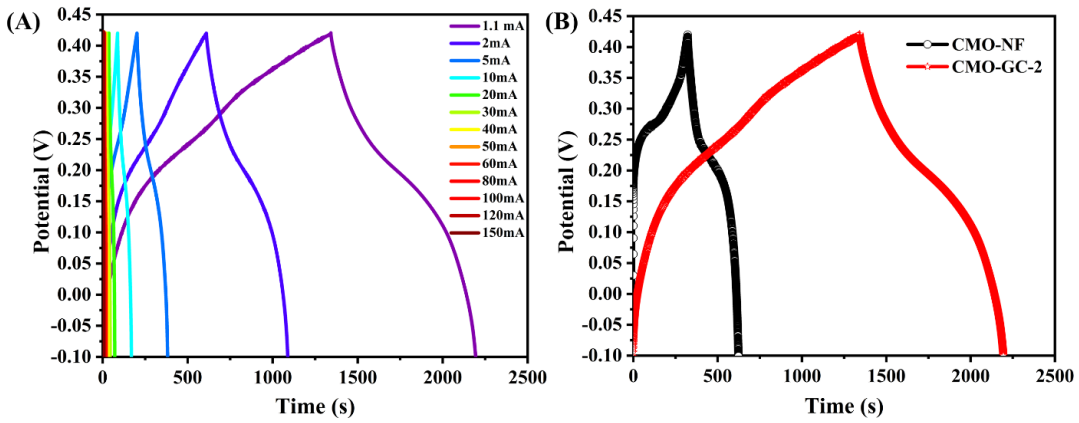

Figure 5.25 GCD plot of CMO-GC-2 (A) and GCD comparison of CMO-GC-2 and CMO-NF (B).

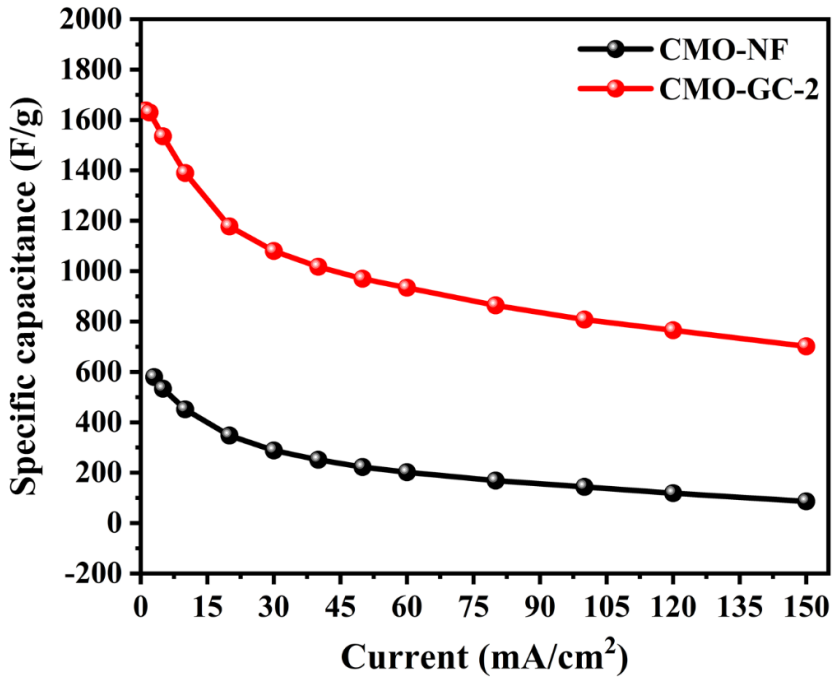

Figure 5.26 Specific capacitance comparison of CMO-NF and CMO-GC-2 electrode.

The increase in charge-discharge time due to the aforementioned reasons, in return, has increased the specific capacitance of the glucose treated electrode. The specific capacitance of as high as 1638 F/g has been achieved for a current density of 1 A/g, which is around three-fold of the specific capacitance of the pristine CMO-NF electrode. For the CMO-GC-2 electrode, the specific capacitance of 1638.17 F/g, 1629.85 F/g, 1535.48 F/g, 1389.66 F/g, 1177.67 F/g is observed for the 1.13 mA/cm^2 (1A/g), 2 mA/cm^2, 5 mA/cm^2, 10mA/cm^2 and 20 mA/cm^2 current densities respectively. Furthermore, the specific capacitance of as high as 612.66 F/g is maintained for the current density of 200 mA/cm^2 (177 A/g). The carbon-cobalt molybdate matrix remains intact up to the very high current density and serves its purpose of superior hybrid supercapacitor material amalgam.

To choose the best out of the glucose treatment, CMO-GC electrodes with different concentrations of glucose were fabricated. The electrode prepared with the glucose concentration of 1mmol, 3mmol, and 4mmol were named CMO-GC-1, CMO-GC-3, and CMO-GC-4 respectively. The CV and GCD analysis for each of the as-fabricated electrodes were performed under the same conditions bound by the same electrochemical and experimental values. Because the CV and GCD characteristic plots are hugely affected by the mass of the active material, and because all electrodes were prepared separately, the mass of the active material in all of the electrodes is different from one another. The GCD plot of all the electrodes at the current density of 1 A/g has been plotted as shown in Figure 5.27(A) to make the data more comparable.

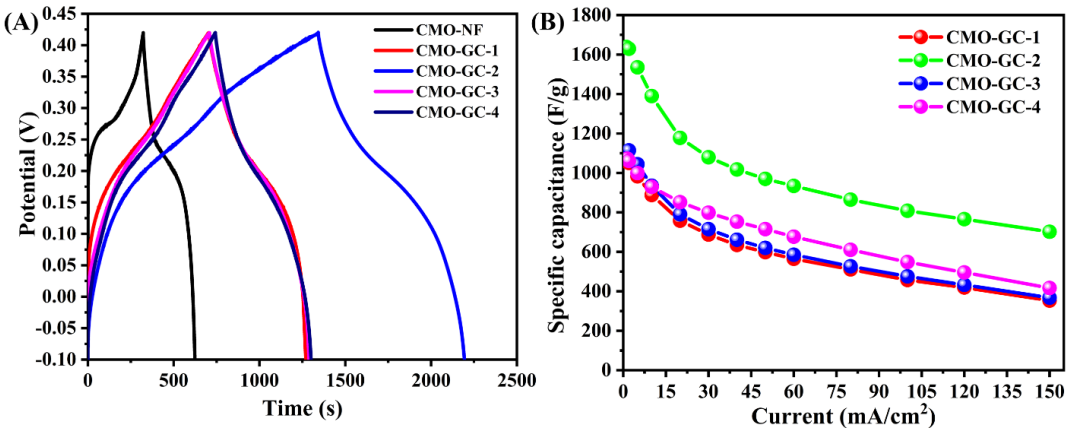

Figure 5.27 GCD comparison for different electrodes at 1A/g (A) and specific capacitance of respective electrodes (B).

A stark difference can be observed between four glucose treated CMO-GC electrodes. The 2mmol glucose treated electrode shows the highest charge-discharge time, which we believe is due to the synergetic effect of overall carbon treatment and rather attractively formed carbon nanospheres that cover the surface of the electrode as shown in the SEM image. Besides having the smallest surface to volume ratio and hence a large surface area, the carbon nanospheres have various advantages such as uniformity,

high thermal stability, and excellent conductivity. Consequently, having a carbon nanospheres on an electrode surface greatly boosts the charge-discharge time and in turn a specific capacitance of the electrode. The comparative specific capacitance of various electrodes can be seen in Figure 5.27(B) . As we saw earlier in SEM images, all the CMO-GC electrodes have a different surface morphology. The absence of a carbon nanosphere on the CMO-GC-1 electrode could be the reason for its lower specific capacitance. Similarly, few carbon nanospheres presence in the CMO-GC-3 electrode could be the reason for slightly better specific capacitance. And the presence of carbon nanospheres but a broken one might be the reason a specific capacitance of CMO-GC-4 electrode is higher than previously mentioned two electrodes but lower than the CMO-GC-2. The CMO-GC-2 electrode has a uniformly distributed, rather large number of smooth-edged carbon nanospheres, which we believe is the reason for its highest specific capacitance. In addition to the SEM image, the EDS analysis shows the maximum carbon presence in the CMO-GC-2 electrode. The supplementary carbon presence is believed to facilitates better electrical conductivity and helps for faster charge transfer kinetics. Similarly, for other glucose treated electrodes also, the EDS data support the claim that the amount of carbon presence significantly affects the specific capacitance. Although there are no comparable research data on the use of glucose to enhance the specific capacitance of the $CoMoO_4$ nanoplates, we tried to compare our result with some of the reported ones, that tried to incorporate the carbon or other metal oxide combinations for the specific capacitance improvement of $CoMoO_4$.

Table 5.2 Specific capacitance comparison of CMO-GC-2 electrode with reported electrodes.

S. No.	Electrode configuration	Measurement value	Specific capacitance	Reference
1	$CoMoO_4$/ MWCNTs	0.1 A/g	170 F/g	[163]
2.	$CoMoO_4.0.75H_2O$/PANI	1 A/g	380 F/g	[164]
3.	$CoMoO_4$@Carboncloth	2 A/g	452 F/g	[156]
4.	$CoMoO_40.9H_2O$–rGO	1 A/g	802.2 F/g	[165]
5.	NiO@$CoMoO_4$	0.5 A/g	848 F/g	[166]
6.	$CoMoO_4$@RGO	1 A/g	856.2 F/g	[167]
7.	$CoMoO_4$–$NiMoO_4.xH_2O$	2.5 mA/cm^2	1039 F/g	[168]
8.	Co_3O_4@$CoMoO_4$ core/shell	1 A/g	1040 F/g	[169]
9.	CMO-GC	1 A/g	1638.17 F/g	This work

Long cyclic GCD at higher current density was examined for CMO-NF and CMO-GC-2 electrodes to evaluate the charge stability of the electrode as shown in Figure 5.28. After 3000 cycles, the capacity retention of 86.28 % and 68.18% were observed for CMO-GC-2 and CMO-NF electrodes, respectively. The higher capacity retention of almost 20 % more for the CMO-GC-2 electrode is attributed to the existence of a carbon NSs matrix on the CMO. The carbon-cobalt molybdate matrix remains intact up to the very high current density and serves its purpose of superior hybrid supercapacitor material combination.

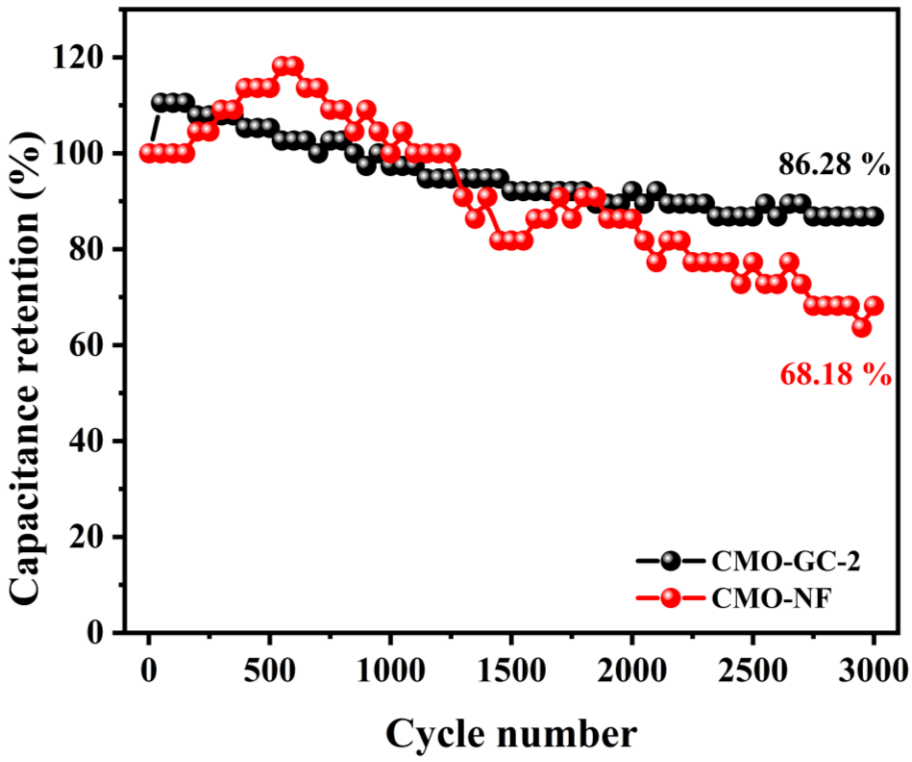

Figure 5.28 Stability test of CMO-GC-2 and CMO-NF electrodes.

The amount of charge-storage occurred at the CMO-GC-2 due to the surface, and intercalation capacitance was determined using Dunn's method, as shown in Figure 5.29(A-D) [170]. Accordance with the Power law ($I = a \times v^b$), The plot of log (i) against the log (v) determined from the CV profiles of CMO-GC-2 is provided in Figure 5.29(A) and the corresponding 'b' value (determined from the linear fit of log v vs. log i) were shown in the inset of Figure 5.29(A). The 'b' value is an essential parameter from the surface and diffusion capacitance of an electrode.

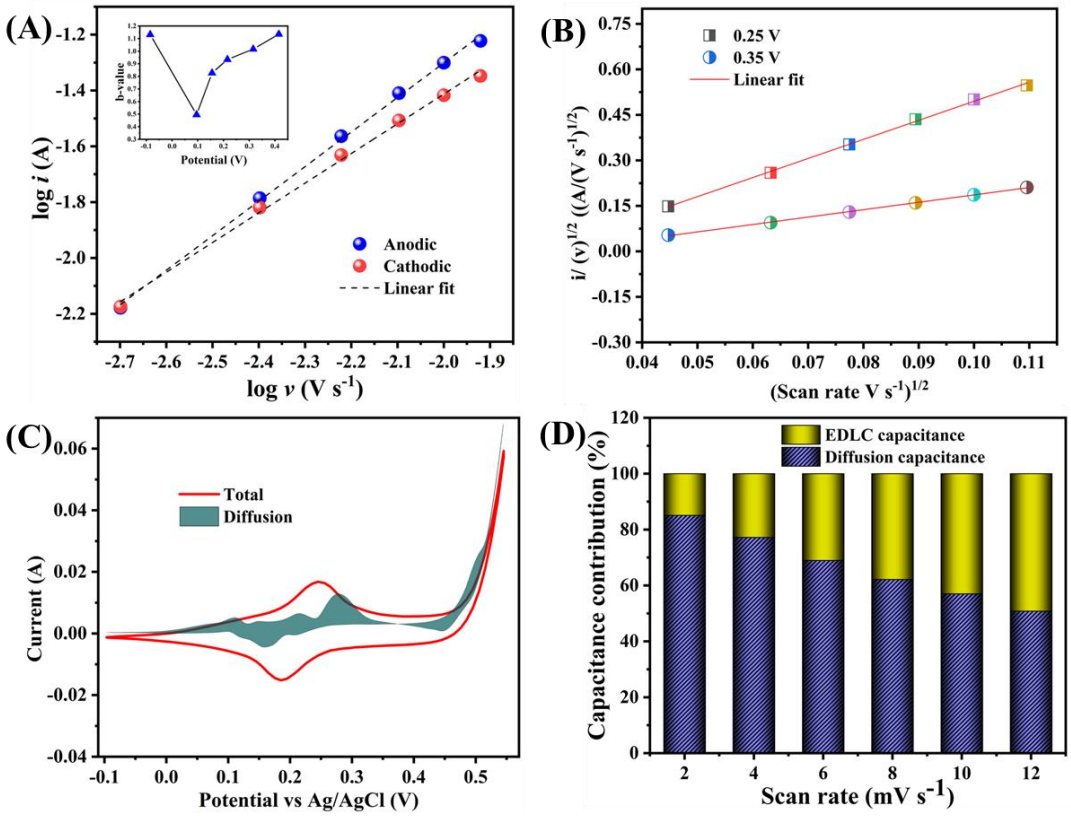

Figure 5.29 The current response against scan rate for CMO-GC-2 electrodes at different voltages, and the inset is b-values (A), CV for differentiating the diffusion-controlled process from the total contribution (B), CV showing the capacitive contribution to total current at select scan rates (C), and Normalized contribution ratio of capacitive capacitance at different scan rates (D).

The 'b' value of 1.1 signifies the dominance of a surface governed reaction in a capacitive process. The 'b' value is obtained to be 0.5 (anodic sweep), which implies the dominance of a diffusion governed reaction of charge-storage. The quantitative analysis of the diffusive and surface controlled capacitance of CMO-GC-2 electrode was derived from the equation $i = k_1v + k_2v^{1/2}$[171]. In this equation, k_1v represents the capacitive contribution, and $k_2v^{1/2}$ stands for the diffusion contribution, where constants k_1 and k_2 can be calculated by plotting $v^{1/2}$ against $i/v^{1/2}$.

Figure 5.29(C) displays the current contribution from diffusion-controlled capacitance (shaded area) over the total current contribution of the CMO-GC-2 electrode. The calculated diffusion-controlled capacitance of the CMO-GC-2 electrode is about 85.1 % at a scan rate of 2.0 mV/s (Figure 5.29(D)). The obtained capacitive contributions are 14.9, 22.8, 31.0, 37.8, 43.0, and 49.2% at the scan rates of 2, 4, 6, 8, 10, 12 mV/s, respectively. With an increase in scan rate from 2 to 12 mV/s, the contribution of diffusion capacitance decreased from 85.1 to 50.8% as a result of an increase in the contribution of surface capacitance at high scan rates, which is explicit from Figure 5.29(D). This analysis indicated that the mechanism of charge-storage at the corban grown CMO-GC-2 electrode is due to the combination of both diffusion capacitance and surface capacitance. The enhanced charge transfer kinetics and fast surface capacitive storage of the CMO-GC-2 electrode can be attributed to the effective surface area of carbon nanospheres over the $CoMoO_4$ NPs, the intrinsic pathways between the NPs and the close contact of $CoMoO_4$ with conductive carbon [172]. Overall, the prepared CMO-GC-2 shows its superior performance as a positive electrode for a supercapacitor device.

5.2.3. Electrochemical characterization results of supercapacitor device

After electrochemical characterization of each electrode, the CMO-GC-2 was identified as the best one and was used in a further study of supercapacitor device fabrication and its electrochemical properties assessment. To fabricate the supercapacitor device CMO-GC-2 was used as a positive electrode and activated carbon on nickel foam (AC-NF) was used as a negative electrode. The polypropylene film was used as a separator. Similar to the previous experimental conditions, 2M KOH aqueous

solution was used as an electrolyte. Following mass balance equation was used to calculate the actual mass of the activated carbon needed to fabricate a supercapacitor device,

$$\frac{m^-}{m^+} = \frac{C^+ \times \Delta V^+}{C^- \times \Delta V^-} \quad \text{.....(13)}$$

Where, m^- is the active material mas of the negative electrode, m^+ is the active material mas of the positive electrode, C^+ is the specific capacitance of the positive electrode, C^- is the specific capacitance of the negative electrode, ΔV^+ is the potential window for the positive electrode at which the specific capacitance was calculated and ΔV^- is the potential window for the negative electrode at which the specific capacitance was calculated. To calculate the specific capacitance of the negative electrode, GCD was performed under 3 electrode system with AC-NF as a working electrode, Ag/AgCl as a reference electrode, and platinum as a counter electrode. The GCD result of the AC-NF electrode is shown in Figure 30(A). In addition to the GCD, CV analysis was also performed for the AC-NF electrode to confirm its EDLC nature, and the obtained plot is shown in Figure 30(B).

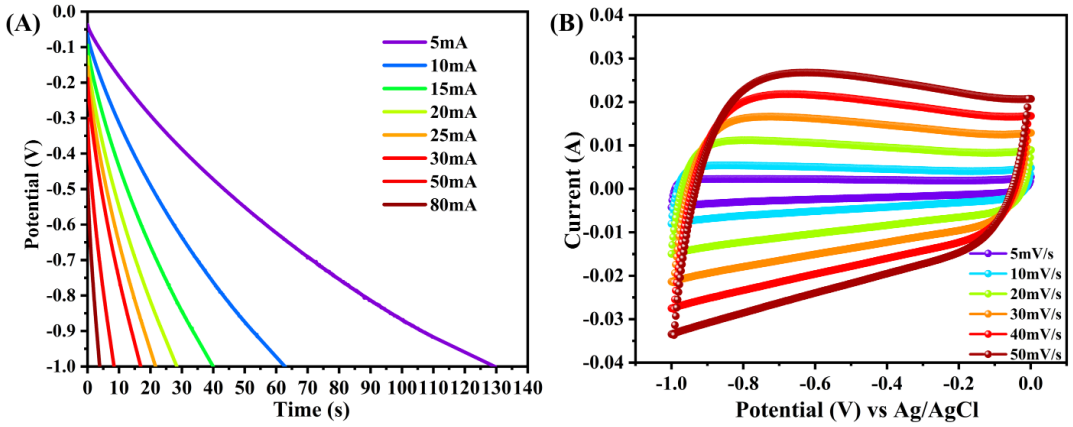

Figure 5.30 GCD plot of AC-NF (A) and CV plot of AC-NF (B).

Both GCD and CV plots are in good agreement with the result of our previously reported article and follow the EDLC nature, hence can be a perfect electrode element for supercapacitor purpose. Several AC-NF electrodes with the same AC weight percentage were fabricated and check for the specific capacitance. The optimized specific capacitance obtained was 129.75 F/g at 1A/g current density. With this specific capacitance, the weight of the activated carbon needed for a supercapacitor fabrication is calculated to be 7.2 mg. Hence, the hybrid supercapacitor device is fabricated and tested with CV, GCD, and EIS analysis. The CV and GCD analyses were done within the potential window of 0 V to 1.5 V. The GCD plot at various current densities can be seen in Figure 5.31 (A). Rectangular-shaped GCD plots were obtained with evenly distributed charge-discharge profiles. Furthermore, the CV plot of the same device in Figure 5.31(B) shows proportioned curves with a consistent increment in the area. No sudden change in the appearance of the CV plots even at a higher scan rate suggests the good electrochemical reversibility of the device.

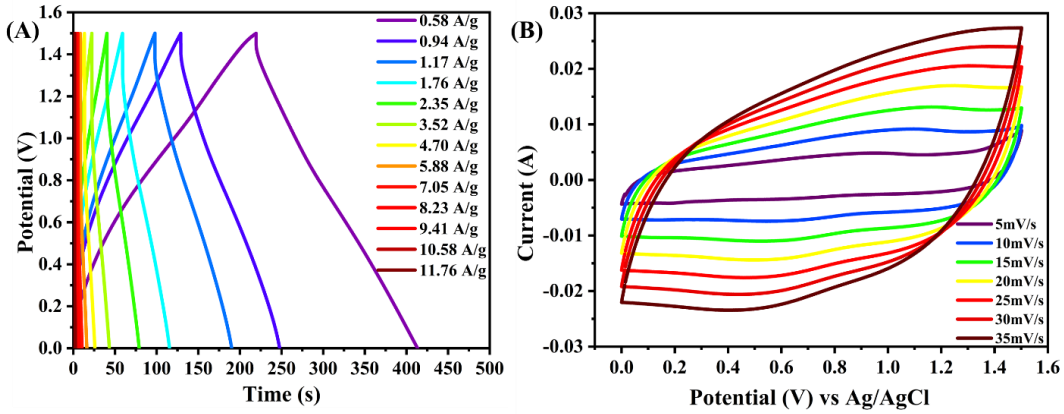

Figure 5.31 GCD plot of the hybrid supercapacitor device (A) and CV plot of the same device (B).

Energy density and power density are the most important parameters to characterize the energy storage devices. We calculated energy density and power density for our hybrid supercapacitor device using the following formulas,

$$E = \frac{1}{2} C_s V^2 \quad \text{.....(14)}$$

$$P = \frac{E}{\Delta t} \quad \text{.....(15)}$$

Where E is the energy density, C_s is the specific capacitance of the device, V is the potential window, P is the power density, and Δt is the discharge time. A Ragone plot is plotted using equations 6 and 7 and can be seen in Figure 5.32.

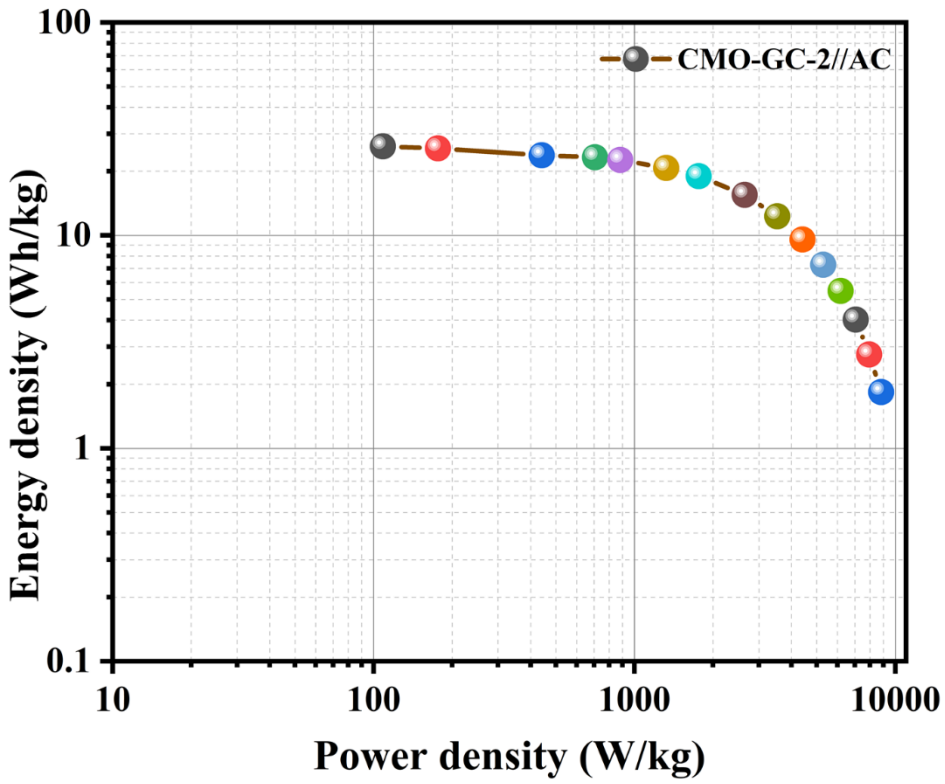

Figure 5.32 Ragone plot of a fabricated hybrid supercapacitor device.

The CMO-GC-2//AC exhibits a maximum energy density of 26.1 Wh/kg with the corresponding power density of 108.5 W/kg as shown in Figure 5.32. Similarly, the

energy density of 9.55 Wh/kg is preserved at a power density of 4411.8 W/kg. Even at the higher power density of 8823.5 W/kg, the device still retained the energy density of 2 Wh/kg at a current density of 10 A/g. The energy density and power density of ASC device are significantly higher compared to the reported transition metal oxide derived ASC device as shown in the table 5.3.

Table 5.3 ASC device performance comparison with reported ones.

S. No.	ASC device	Potential window (V)	Energy density (Wh/kg)	Power density (W/kg)	Ref
1	$CoMoO_4$-HMPA/NF//AC	1.6	0.321 mWh/cm^2	1.7 mW/cm	[160]
2.	$NiCo_2O_4$ NG@CF	1.65	6.61	425	[173]
3.	NiCoMoCuO	1.6	13.99	340.4	[174]
4.	$CoMoO_4$–3D Graphene//AC	1.8	21.1	300	[122]
5.	$NiCo_2O_4$@$MnMoO_4$ CSNAs//AC	1.6	15	6734	[175]
6.	$ZnCo_2O_4$/H:ZnO NRs//AC	1.5	3.75	653.3	[176]
7.	$CoMoO_4$-$NiMoO_4$//AC	1.4	16	1600	[168]
8.	α-$CoMoO_4$//AC	1.2	14.5	1000	[177]
9.	$CoMoO_4$//r-GO	1.5	8.17	187.5	[123]
10.	CMO-GC//AC	1.5	26.1	8823.5	This work

On the other hand, to analyze the stability of the fabricated device, the stability test was performed at a high current density of around 10 A/g. Figure5.33 shows the result of the long-term stability of CMO-GC-2//AC up to the 5000 repeated charge-discharge process. More than 87% of the initial specific capacitance was retained after 5000 cycles. The significant loss of C_s could be due to the peeling off the loosely bound

particles on the surface during continuous ion insertion/desertion. The capacitive retention reached 90% after 2000 cycles, which suggest that the loosely bound particles peeled off and deteriorate of the carbon particles on the surface completed before 2000 cycles. Therefore, the capacitive retention retained after 2000 cycles, which also confirmed by the post-mortem FE-SEM analysis of the electrode after the cyclic test. This result demonstrated the excellent stability of the fabricated ASC device. It opened a possibility for a supercapacitor device that can be fabricated with a much easier chemical synthesis process and with an efficient, eco-friendly, and economical precursors such as glucose.

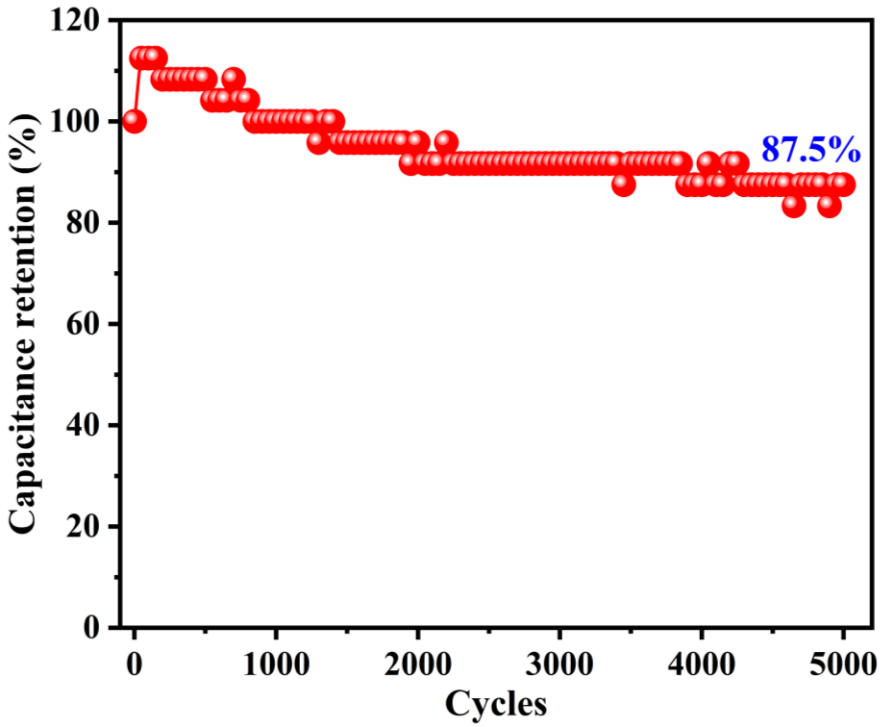

Figure 5.33 Stability test of the hybrid supercapacitor device.

Electrochemical impedance spectroscopy was performed to analyze the charge transfer characteristics of the device. Figure 5.34 shows the Nyquist plot of the device before and after the 5000 cycles stability test. The inset of the figure is a circuit fitted

with equivalent electrical components. As we can see in the figure both curves are composed of a semicircle in higher frequency region and linear line in the lower frequency region. The semicircle represents the charge transfer resistance (R_{ct}) of the interface between the electrode and electrolyte [148]. The linear line in the lower frequency region represents the Warburg impedance and corresponds to the diffusion of OH^- ion into the pores of the CMO-GC electrode [149]. The equivalent series resistance (R_s) corresponds to the combined resistance of active material, ionic resistance of the electrolyte, and active material/current collector interface [150]. Respective values for the equivalent electrical component can be seen in table 5.4. No significant difference in the charge transfer resistance and equivalent series resistance suggests that the contact between the active material and the current collector has not weakened substantially.

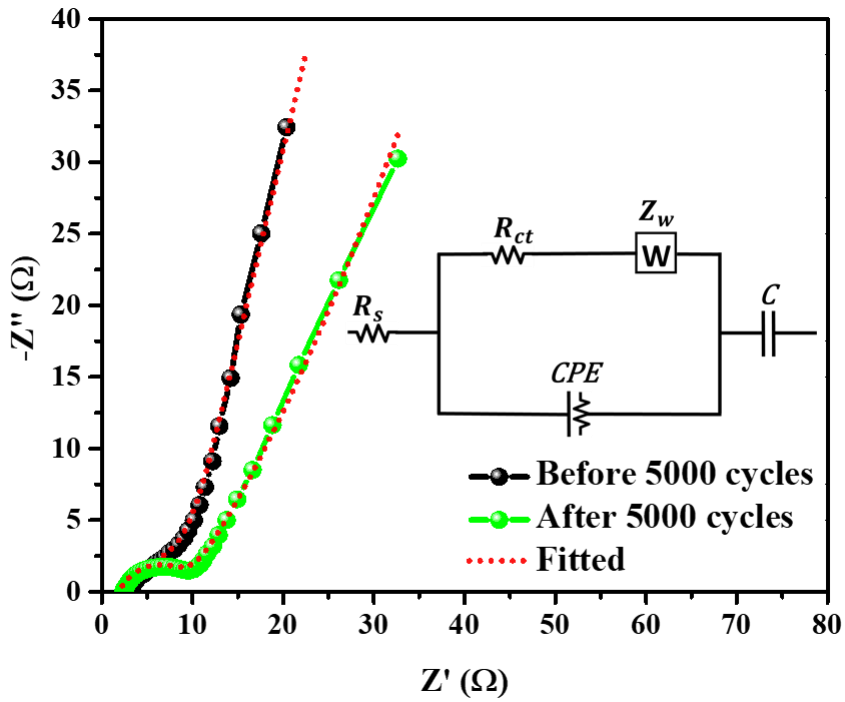

Figure 5.34 EIS of the supercapacitor device before and after 5000 cycles.

Table 5.4 EIS equivalent electrical component values for the ASC device before and after 5000 cycles.

	R_s	R_{ct}	Z_w	CPE	C
Before 5000 cycles	3.3 Ohm	7.2 Ohm	9.0 mMho	0.9 mMho	1.4 mF
After 5000 cycles	2.1 Ohm	8.0 Ohm	100.0 mMho	3.0 mMho	1.3 F

To understand the electrochemical performance and reaction kinetics after stability test, FE-SEM and XPS analysis of the electrode was performed. Figure 5.35 (A-C) represents the FE-SEM macroscopic image of CMO-GC-2 electrode after the

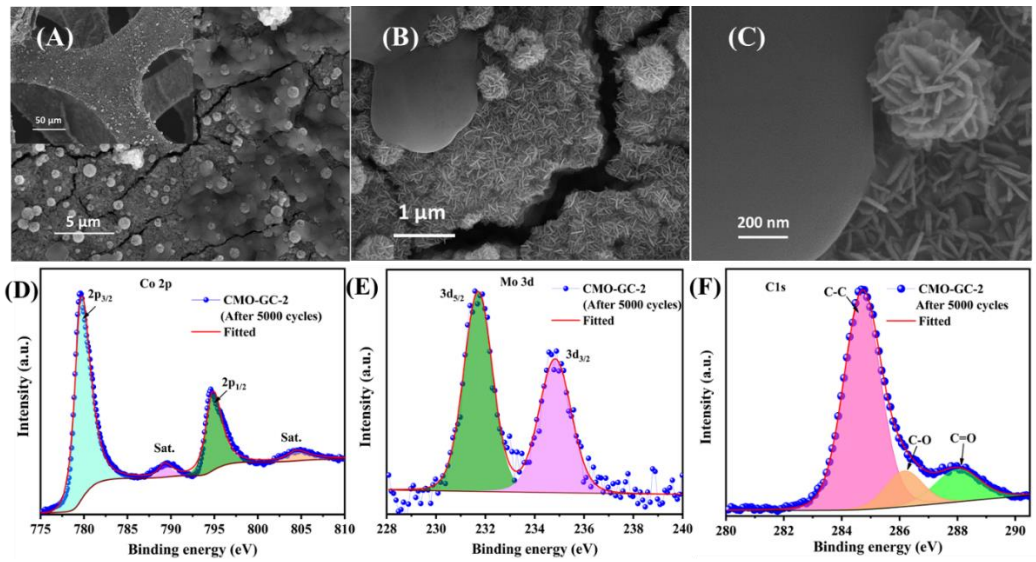

Figure 5.35 FE-SEM images of CMO-GC-2 electrode after 5000 GCD cycles (A-C), and XPS core-level spectra: Co 2p core level spectrum (D), Mo 3d core-level spectrum (E), and C 1s core-level spectrum (F) of CMO-GC-2 electrode after 5000 GCD cycles.

cyclic test. It clearly shows the deceases of carbon nanospheres and the few layers of

carbon present on the CMO-NF. No significant morphology modification of $CoMoO_4$ nanoplates observed on the surface, which means the considerable amount of carbon peeled-off and structural collapse occurs during charge-discharge cycles due to weak mechanical binding. The embedded carbon NSs and thin carbon layer provide the structural stability of $CoMoO_4$ NPs during the cyclic test. XPS measures the chemical characteristic of elements after the cyclic test. The XPS core level spectrum of Co 2p observed two peaks at 780.0 eV, and 794.7 eV, which corresponds to the 2 $p_{3/2}$ and 2 $p_{1/2}$ of elemental state of Co^{2+} as shown in Figure 5.35(D). Figure 5.35(E) shows that the core level spectrum of the Mo 3d exhibits at two peaks associated with the $3d_{3/2}$ and $3d_{5/2}$ of Mo^{6+} which are observed at 232.0 and 235.1 eV, respectively. The corresponding satellite peaks are observed at 285.5 eV and 803.1 eV of CMO-NF, which associated with the Co 2p. There are no significant defects in the crystalline state of the $CoMoO_4$ NPs by the ions and charge during GCD cycles. Moreover, C 1s core-level spectrum of CMO-GC-2 shows the three peaks at 284.6 eV, 285.5 eV, and 288.0 eV, which are associated with the graphitic(C-C), hydroxyl(C-O), and keto(C=O) respectively (Figure 5.35(F)). The observed results suggest the presence of intact carbon on the surface of the CMO NPs, which favors the long-term stability of the electrode

6. CONCLUSIONS AND FUTURE DIRECTION

$CoMoO_4$ and CoMoS were successfully synthesized with relatively effortless experimental conditions for the purpose of superior LIB anode materials. CoMoS was carbonized using dopamine as a carbon source and physical characterization results show a good amount of carbon presence. Pristine CoMoS and carbonized CoMoS (CoMoS@NC) were used as electrode materials and CR2032 half cells were fabricated using respective materials. Thus prepared electrodes were checked for their specific charge-discharge capacity upon numerous cycles. Also, the charge-discharge capacity was measured for different current densities. The excellent discharge capacity of around 420 mAh/g and 720 mAh/g for CoMoS and CoMoS@NC respectively were obtained for the 100^{th} cycle even at the high current density of 200 mA/g. Also, the charge-discharge at different current densities results show an excellent capacity retention ability of both the electrode. To summarize the results, CoMoS and CoMoS@NC could be excellent anode material alternatives for LIBs. Also, dopamine could be an outstanding carbon precursor to fabricate the carbonaceous electrode for LIB applications.

The self-grown $CoMoO_4$ nanoplates on nickel foam were successfully synthesized as a supercapacitor electrode. As synthesized CMO-NF electrode was carbonized with different concentrations of glucose as a carbon precursor. 2 mmol glucose was identified as the optimum concentration that can yield the carbon with the beautiful surface morphology, which in turn gave the best specific capacitance value among all the carbon treated electrodes. The hybrid supercapacitor device was fabricated with 2 mmol glucose treated CMO-NF electrode and activated carbon coated electrode. The energy density and power density of the device were calculated and

found to be around 20 Wh/kg for the power density of 82 W/kg. This is an excellent result compared to the EDLC type supercapacitor device and many supercapacitor devices fabricated with similar material. Also, the outstanding rate capability of the device was observed as it retained more than 87 % of the initial capacity even after 5000 cycles of charge-discharge cycles, which makes our device an excellent hybrid supercapacitor device candidate.

To summarize, this thesis work has aimed to provide some insight into possible ways of improving the performance of conventional energy storage devices such as supercapacitor and LIBs. CoMoO4 has been presented as a base material for both supercapacitor and LIB work owing to its high theoretical capacity and ease of access. Different electrode fabrication techniques were practiced such as self-grown and slurry-coating methods for supercapacitor and battery work, respectively. Furthermore, the methods for carbon incorporation into the active material composite are also different. The variations in the methodologies provided an opportunity to work with different elemental compositions and enabled us to come up with some excellent results on both energy storage devices. The use of glucose and dopamine as a carbonaceous material to enhance the performance of energy storage devices has presented rather attractively through the series of experimental results. Since our goal was to synthesize highly efficient energy storage applications that ultimately promote green energy solutions, the use of eco-friendly carbon precursors significantly favored our findings in the direction of green energy. Both carbon precursors enhanced the energy storage ability of ES devices by boosting the electrochemical performance of active materials. Hence, it can collectively be said that the high energy density and high-power density ES device were fabricated successfully.

Also, working with two different carbonaceous materials presented the possibility of their interchangeability or mixing with different materials for a variety of ES applications. In the future, one can either make a carbonaceous battery electrode or a carbonaceous supercapacitor electrode with glucose or dopamine as a carbon precursor, respectively. Furthermore, by varying the parameters such as carbon treatment time, the carbon precursor concentrations, the synthesis temperature, etc., advanced future research can be performed.

7. REFERENCES

1 P. M. Vitousek, H. A. Mooney, J. Lubchenco and J. M. Melillo, Science (80-.)., 1997, 277, 494–499.

2 H. Tian, C. Lu, P. Ciais, A. M. Michalak, J. G. Canadell, E. Saikawa, D. N. Huntzinger, K. R. Gurney, S. Sitch, B. Zhang, J. Yang, P. Bousquet, L. Bruhwiler, G. Chen, E. Dlugokencky, P. Friedlingstein, J. Melillo, S. Pan, B. Poulter, R. Prinn, M. Saunois, C. R. Schwalm and S. C. Wofsy, Nature, 2016, 531, 225–228.

3 M. Collins, S. Il An, W. Cai, A. Ganachaud, E. Guilyardi, F. F. Jin, M. Jochum, M. Lengaigne, S. Power, A. Timmermann, G. Vecchi and A. Wittenberg, Nat. Geosci., 2010, 3, 391–397.

4 S. Pacala and R. Socolow, Science (80-.)., 2004, 305, 968–972.

5 E. L. Schneider, C. T. Oliveira, R. M. Brito and C. F. Malfatti, J. Power Sources, 2014, 262, 1–9.

6 B. E. Conway, Electrochem. Supercapacitors, 1999, 11–31.

7 M. Winter and R. J. Brodd, Chem. Rev., 2004, 104, 4245–4269.

8 J. B. Goodenough and Y. Kim, Chem. Mater., 2010, 22, 587–603.

9 V. Etacheri, R. Marom, R. Elazari, G. Salitra and D. Aurbach, Energy Environ. Sci., 2011, 4, 3243–3262.

10 T. Christen and M. W. Carlen, J. Power Sources, 2000, 91, 210–216.

11 C. Julien, A. Mauger, A. Vijh and K. Zaghib, Lithium Batter. Sci. Technol., 2015, 1–27.

12 D. Linden and T. B. Reddy, HANDBOOK OF BATTERIES, 2002.

13 J.-M. Tarascon and M. Armand, Nature, 2001, 414, 359–367.

14 R. J. Brodd, Lithium-Ion Batter. Sci. Technol., 2009, 1–7.

15 L. Lu, X. Han, J. Li, J. Hua and M. Ouyang, J. Power Sources, 2013, 226, 272–288.

16 C. Julien, A. Mauger, A. Vijh and K. Zaghib, Lithium Batteries: Science and Technology, 2015.

17 T. Pandolfo, V. Ruiz, S. Sivakkumar and J. Nerkar, Supercapacitors Mater. Syst. Appl., 2013, 69–109.

18 B. E. Conway, Electrochem. Supercapacitors, 1999, 87–104.

19 G. Z. Chen, Prog. Nat. Sci. Mater. Int., 2013, 23, 245–255.

20 D. Petreus, D. Moga, R. Galatus and R. A. Munteanu, Adv. Electr. Comput. Eng., 2008, 8, 15–22.

21 R. Kotz and M. Carlen, Electrochem. Acta, 2000, 45, 2483–2498.

22 G. Wang, L. Zhang and J. Zhang, Chem. Soc. Rev., 2012, 41, 797–828.

23 E. Frackowiak and F. Beguin, Carbon N. Y., 2001, 39, 937–950.

24 A. Burke, J. Power Sources, 2000, 91, 37–50.

25 Y. Simon, P., and Gogotsi, Science (80-.)., 2014, 343, 1210–1211.

26 P. Simon and Y. Gogotsi, Nat. Mater., 2008, 7, 845–854.

27 S. Najib and E. Erdem, Nanoscale Adv., 2019, 1, 2817–2827.

28 B. E. Conway, Electrochem. Supercapacitors, 1999, 221–257.

29 T. Brousse, D. Bélanger and J. W. Long, J. Electrochem. Soc., 2015, 162, A5185–A5189.

30 E. Frackowiak, Supercapacitors Mater. Syst. Appl., 2013, 207–237.

31 Y. Zhang, H. Feng, X. Wu, L. Wang, A. Zhang, T. Xia, H. Dong, X. Li and L. Zhang, Int. J. Hydrogen Energy, 2009, 34, 4889–4899.

32 J. Liu, J. Jiang, C. Cheng, H. Li, J. Zhang, H. Gong and H. J. Fan, Adv. Mater.,

2011, 23, 2076–2081.

33 M. D. Stoller, S. Park, Y. Zhu, J. An and R. S. Ruoff, Nano Lett., 2008, 8, 3498–3502.

34 M. Mastragostino, C. Arbizzani and F. Soavi, J. Power Sources, 2001, 98, 812–815.

35 C. Arbizzani, M. Mastragostino and L. Meneghello, Electrochim. Acta, 1996, 41, 21–26.

36 J. P. Zheng, P. J. Cygan and T. R. Jow, J. Electrochem. Soc., 1995, 142, 2699–2703.

37 J. P. Zheng and T. R. Jow, J. Electrochem. Soc., 1995, 142, L6.

38 D. P. Dubal, O. Ayyad, V. Ruiz and P. Gomez-Romero, Chem. Soc. Rev., 2015, 44, 1777–1790.

39 K. Naoi, S. Ishimoto, J. I. Miyamoto and W. Naoi, Energy Environ. Sci., 2012, 5, 9363–9373.

40 B. E. Conway and W. G. Pell, J. Solid State Electrochem., 2003, 7, 637–644.

41 M. S. Halper and J. C. Ellenbogen, .

42 T. Liangliang and J. Chunyang, Prog. Chem., 2010, 22, 1610–1618.

43 A. Laforgue, P. Simon, J. F. Fauvarque, M. Mastragostino, F. Soavi, J. F. Sarrau, P. Lailler, M. Conte, E. Rossi and S. Saguatti, J. Electrochem. Soc., 2003, 150, A645.

44 E. Frackowiak, V. Khomenko, K. Jurewicz, K. Lota and F. Béguin, J. Power Sources, 2006, 153, 413–418.

45 E. Frackowiak, K. Jurewicz, S. Delpeux and F. Béguin, J. Power Sources, 2001, 97–98, 822–825.

46 W. Zuo, R. Li, C. Zhou, Y. Li, J. Xia and J. Liu, Adv. Sci., 2017, 4, 1600539.

47 J. B. Goodenough and K. S. Park, J. Am. Chem. Soc., 2013, 135, 1167–1176.

48 Nature, 2001, 414, 359–367.

49 J. O'Heir, Mech. Eng., 2017, 139, 10–11.

50 Dominic A. Notter, Marcel Gauch, Rolf Widmer, Patrick Wäger, Anna Stamp, Rainer Zah and Hans- Jörg Althaus, Environ. Sci. Technol., 2010, 44, 43.

51 L. A. W. Ellingsen, G. Majeau-Bettez, B. Singh, A. K. Srivastava, L. O. Valøen and A. H. Strømman, J. Ind. Ecol., 2014, 18, 113–124.

52 M. S. WHITTINGHAM, Science (80-.)., 1976, 192, 1126–1127.

53 M. S. Whittingham, Chem. Rev., 2004, 104, 4271–4301.

54 K. Mizushima, P. C. Jones, P. J. Wiseman and J. B. Goodenough, Mater. Res. Bull., 1980, 15, 783–789.

55 C. Julien, J. P. Pereira-Ramos and A. Momchilov, New Trends in Intercalation Compounds for Energy Storage, Springer Netherlands, Dordrecht, 2002.

56 A. Du Pasquier, I. Plitz, S. Menocal and G. Amatucci, J. Power Sources, 2003, 115, 171–178.

57 J. R. Dahn, E. W. Fuller, M. Obrovac and U. von Sacken, Solid State Ionics, 1994, 69, 265–270.

58 G. V. Zhuang, G. Chen, J. Shim, X. Song, P. N. Ross and T. J. Richardson, J. Power Sources, 2004, 134, 293–297.

59 A. R. Armstrong and P. G. Bruce, Nature, 1996, 381, 499–500.

60 N. Yabuuchi and T. Ohzuku, J. Power Sources, 2003, 119–121, 171–174.

61 A. Yamada, S. C. Chung and K. Hinokuma, J. Electrochem. Soc., 2001, 148, A224.

62 M. Winter, J. O. Besenhard, M. E. Spahr and P. Novák, Adv. Mater., 1998, 10, 725–763.

63 N. A. Kaskhedikar and J. Maier, Adv. Mater., 2009, 21, 2664–2680.

64 C. Julien, A. Mauger, A. Vijh and K. Zaghib, Lithium Batteries: Science and Technology, 2015.

65 X. Yuan, H. Liu and J. Zhang, Lithium-Ion Batter. Adv. Mater. Technol., 2016, 1–428.

66 X. Xu, W. Liu, Y. Kim and J. Cho, Nano Today, 2014, 9, 604–630.

67 M. R. Gao, Y. F. Xu, J. Jiang and S. H. Yu, Chem. Soc. Rev., 2013, 42, 2986–3017.

68 M. Xu, T. Liang, M. Shi and H. Chen, Chem. Rev., 2013, 113, 3766–3798.

69 M. Chhowalla, H. S. Shin, G. Eda, L. J. Li, K. P. Loh and H. Zhang, Nat. Chem., 2013, 5, 263–275.

70 E. Benavente, M. A. Santa Ana, F. Mendizábal and G. González, Coord. Chem. Rev., 2002, 224, 87–109.

71 C. Zhu, P. Kopold, W. Li, P. A. van Aken, J. Maier and Y. Yu, Adv. Sci., 2015, 2, 1–8.

72 R. Tenne, Angew. Chemie - Int. Ed., 2003, 42, 5124–5132.

73 Q. Wang and J. Li, J. Phys. Chem.C, 2007, 111, 1675–1682.

74 Y. C. Lin, W. Zhang, J. K. Huang, K. K. Liu, Y. H. Lee, C. Te Liang, C. W. Chu and L. J. Li, Nanoscale, 2012, 4, 6637–6641.

75 H. Liu, D. Su, R. Zhou, B. Sun, G. Wang and S. Z. Qiao, Adv. Energy Mater., 2012, 2, 970–975.

76 X. Zhang, X. Li, J. Liang, Y. Zhu and Y. Qian, Small, 2016, 12, 2484–2491.

77 S. Ding, D. Zhang, J. S. Chen and X. W. Lou, Nanoscale, 2012, 4, 95–98.

78 J. M. Yan, H. Z. Huang, J. Zhang, Z. J. Liu and Y. Yang, J. Power Sources, 2005, 146, 264–269.

79 Y. Zhou, D. Yan, H. Xu, S. Liu, J. Yang and Y. Qian, Nanoscale, 2015, 7, 3520–3525.

80 Y. Zhang, Q. Zhou, J. Zhu, Q. Yan, S. X. Dou and W. Sun, Adv. Funct. Mater., 2017, 27, 1–34.

81 Y. Gu, Y. Xu and Y. Wang, ACS Appl. Mater. Interfaces, 2013, 5, 801–806.

82 Y. Du, X. Zhu, X. Zhou, L. Hu, Z. Dai and J. Bao, J. Mater. Chem. A, 2015, 3, 6787–6791.

83 J. Tang, Y. Ge, J. Shen and M. Ye, Chem. Commun., 2016, 52, 1509–1512.

84 S. Peng, L. Li, C. Li, H. Tan, R. Cai, H. Yu, S. Mhaisalkar, M. Srinivasan, S. Ramakrishna and Q. Yan, Chem. Commun., 2013, 49, 10178–10180.

85 V. N. Bui, D. Laurenti, P. Afanasiev and C. Geantet, Appl. Catal. B Environ., 2011, 101, 239–245.

86 B. Yoosuk, J. H. Kim, C. Song, C. Ngamcharussrivichai and P. Prasassarakich, Catal. Today, 2008, 130, 14–23.

87 L. Yu, B. Y. Xia, X. Wang and X. W. Lou, Adv. Mater., 2016, 28, 92–97.

88 F. Zheng, N. Huang, R. Peng, Y. Ding, G. Li, Z. Xia, P. Sun, X. Sun and J. Geng, Electrochim. Acta, 2018, 263, 328–337.

89 N. Dominguez, B. Torres, L. A. Barrera, J. E. Rincon, Y. Lin, R. R. Chianelli, M. A. Ahsan and J. C. Noveron, ACS Omega, 2018, 3, 10243–10249.

90 S. H. Yang, S. K. Park, J. K. Kim and Y. C. Kang, J. Mater. Chem. A, 2019, 7, 13751–13761.

91 G. Guo, Z. Song, C. Cong and K. Zhang, J. Nanoparticle Res., 2007, 9, 653–656.

92 Y.-H. Dai, L.-B. Kong, K. Yan, M. Shi, T. Zhang, Y.-C. Luo and L. Kang, 2016, 6, 7633–7642.

93 F. Wang, G. Li, J. Zheng, J. Ma, C. Yang and Q. Wang, RSC Adv., 2018, 8, 38945–38954.

94 H. Li, Y. Zhao and C. A. Wang, J. Mater. Sci. Mater. Electron., 2018, 29, 13703–13708.

95 Y. H. Dai, L. Bin Kong, K. Yan, M. Shi, T. Zhang, Y. C. Luo and L. Kang, RSC Adv., 2016, 6, 7633–7642.

96 R. Li, K. Parvez, F. Hinkel, X. Feng and K. Müllen, Angew. Chemie - Int. Ed., 2013, 52, 5535–5538.

97 K. Liu, W. Z. Wei, J. X. Zeng, X. Y. Liu and Y. P. Gao, Anal. Bioanal. Chem., 2006, 385, 724–729.

98 R. Liu, S. M. Mahurin, C. Li, R. R. Unocic, J. C. Idrobo, H. Gao, S. J. Pennycook and S. Dai, Angew. Chemie - Int. Ed., 2011, 50, 6799–6802.

99 J. Yan, H. Lu, Y. Huang, J. Fu, S. Mo, C. Wei, Y. E. Miao and T. Liu, J. Mater. Chem. A, 2015, 3, 23299–23306.

100 A. Postma, Y. Yan, Y. Wang, A. N. Zelikin, E. Tjipto and F. Caruso, Chem. Mater., 2009, 21, 3042–3044.

101 A. Postma, Y. Yan, Y. Wang, alexender n. Zelikin, E. Tjipto and F. Caruso, .

102 W. Gong, W. Chen, J. He, Y. Tong, C. Liu, L. Su, B. Gao, H. Yang, Y. Zhang and X. Zhang, Carbon N. Y., 2015, 83, 275–281.

103 X. Yao, C. Zhao, J. Kong, H. Wu, D. Zhou and X. Lu, Chem. Commun., 2014, 50, 14597–14600.

104 J. Kong, W. A. Yee, L. Yang, Y. Wei, S. Lei Phua, H. Guan Ong, J. Ming Ang, X. Li and X. Lu, Chem. Commun., 2012, 48, 10316–10318.

105 H. Li, L. Shen, K. Yin, J. Ji, J. Wang, X. Wang and X. Zhang, J. Mater. Chem. A, 2013, 1, 7270–7276.

106 C. Liu, J. Wang, J. Li, R. Luo, J. Shen, X. Sun, W. Han and L. Wang, ACS Appl.

Mater. Interfaces, 2015, 7, 18609–18617.

107 H. Xiao, C. Tao, Y. Li, X. Chen, J. Huang and J. Wang, Nanomaterials, 2018, 8, 854.

108 W. Cheng, F. Rechberger, D. Primc and M. Niederberger, Nanoscale, 2015, 7, 13898–13906.

109 R. A. Rightmire, US Pat.

110 M. Endo, T. Takeda, Y. J. Kim, K. Koshiba and K. Ishii, Carbon Sci., 2001, 1, 117–128.

111 I.-H. Kim and K.-B. Kim, J. Electrochem. Soc., 2006, 153, A383.

112 S. Chen, J. Zhu, X. Wu, Q. Han and X. Wang, ACS Nano, 2010, 4, 2822–2830.

113 W. Li, G. Li, J. Sun, R. Zou, K. Xu, Y. Sun, Z. Chen, J. Yang and J. Hu, Nanoscale, 2013, 5, 2901–2908.

114 G. H. Yuan, Z. H. Jiang, A. Aramata and Y. Z. Gao, Carbon N. Y., 2005, 43, 2913–2917.

115 Z. J. Lao, K. Konstantinov, Y. Tournaire, S. H. Ng, G. X. Wang and H. K. Liu, J. Power Sources, 2006, 162, 1451–1454.

116 E. Zhou, L. Tian, Z. Cheng and C. Fu, Nanoscale Res. Lett., 2019, 14, 221.

117 C. Yuan, J. Li, L. Hou, X. Zhang, L. Shen and X. W. Lou, Adv. Funct. Mater., 2012, 22, 4592–4597.

118 B. Liu, B. Liu, Q. Wang, X. Wang, Q. Xiang, D. Chen and G. Shen, ACS Appl. Mater. Interfaces, 2013, 5, 10011–10017.

119 L. Bao, J. Zang and X. Li, Nano Lett., 2011, 11, 1215–1220.

120 D. Chen, Q. Wang, R. Wang and G. Shen, J. Mater. Chem. A, 2015, 3, 10158–10173.

121 D. Guo, H. Zhang, X. Yu, M. Zhang, P. Zhang, Q. Li and T. Wang, J. Mater.

Chem. A, 2013, 1, 7247–7254.

122 X. Yu, B. Lu and Z. Xu, Adv. Mater., 2014, 26, 1044–1051.

123 G. K. Veerasubramani, K. Krishnamoorthy and S. J. Kim, RSC Adv., 2015, 5, 16319–16327.

124 J. Wang, Y. Cheng, Z. Liu, W. Cao, S. Wang and H. Xu, J. Sol-Gel Sci. Technol., 2020, 93, 131–141.

125 Y. She, B. Tang, D. Li, X. Tang, J. Qiu, Z. Shang and W. Hu, Coatings, 2018, 8, 340.

126 P. Zhang, X. Zhang and G. Li, Ionics (Kiel)., 2020, 26, 393–401.

127 I. F. Myronyuk, V. I. Mandzyuk, V. M. Sachko and V. M. Gun'ko, Nanoscale Res. Lett., 2016, 11, 508.

128 H. Guo, X. Qi, L. Li and R. L. Smith, Bioresour. Technol., 2012, 116, 355–359.

129 X. Wang, C. Hu, Y. Xiong, H. Liu, G. Du and X. He, J. Power Sources, 2011, 196, 1904–1908.

130 R. Cui, C. Liu, J. Shen, D. Gao, J. J. Zhu and H. Y. Chen, Adv. Funct. Mater., 2008, 18, 2197–2204.

131 J. Zhao, C. Lai, Y. Dai and J. Xie, Mater. Lett., 2007, 61, 4639–4642.

132 P. Zhang, F. Sun, Z. Shen and D. Cao, J. Mater. Chem. A, 2014, 2, 12873–12880.

133 M. Enterría, F. J. Martín-Jimeno, F. Suárez-García, J. I. Paredes, M. F. R. Pereira, J. I. Martins, A. Martínez-Alonso, J. M. D. Tascón and J. L. Figueiredo, Carbon N. Y., 2016, 105, 474–483.

134 B. G. Rao, D. Mukherjee and B. M. Reddy, in Nanostructures for Novel Therapy, Elsevier, 2017, pp. 1–36.

135 H. Zhong, T. Mirkovic and G. D. Scholes, Compr. Nanosci. Technol., 2011, 1–

5, 153–201.

136 M. K. Devaraju and I. Honma, Adv. Energy Mater., 2012, 2, 284–297.

137 H. Schmalzried, 1976, 233–279.

138 Y. J. Leng, S. H. Chan, S. P. Jiang and K. A. Khor, Solid State Ionics, 2004, 170, 9–15.

139 J. I. Goldstein, D. E. Newbury, P. Echlin, D. C. Joy, C. E. Lyman, E. Lifshin, L. Sawyer and J. R. Michael, Scanning electron microscopy and X-ray microanalysis, 2003.

140 N. Elgrishi, K. J. Rountree, B. D. McCarthy, E. S. Rountree, T. T. Eisenhart and J. L. Dempsey, J. Chem. Educ., 2018, 95, 197–206.

141 P. T. Kissinger and W. R. Heineman, J. Chem. Educ., 1983, 60, 702–706.

142 F. Licht, M. A. Davis and H. A. Andreas, J. Power Sources, 2020, 446, 227354.

143 Y. Shao, M. F. El-Kady, J. Sun, Y. Li, Q. Zhang, M. Zhu, H. Wang, B. Dunn and R. B. Kaner, Chem. Rev., 2018, 118, 9233–9280.

144 L. Wang, X. Cui, L. Gong, Z. Lyu, Y. Zhou, W. Dong, J. Liu, M. Lai, F. Huo, W. Huang, M. Lin and W. Chen, Nanoscale, 2017, 9, 3898–3904.

145 M. S. P. Sudhakaran, G. Gnanasekaran, P. Pazhamalai, S. Sahoo, M. M. Hossain, R. M. Bhattarai, S. J. Kim and Y. S. Mok, ACS Sustain. Chem. Eng., 2019, 7, 14805–14814.

146 A. Kraytsberg and Y. Ein-Eli, Adv. Energy Mater., 2016, 6, 1600655.

147 T. Marks, S. Trussler, A. J. Smith, D. Xiong and J. R. Dahn, 2011, 51–57.

148 A. Eftekhari, J. Mater. Chem. A, 2018, 6, 2866–2876.

149 L. Wang, X. Li, T. Guo, X. Yan and B. K. Tay, Int. J. Hydrogen Energy, 2014, 39, 7876–7884.

150 X. Zhang, J. Luo, P. Tang, X. Ye, X. Peng, H. Tang, S. G. Sun and J. Fransaer,

Nano Energy, 2017, 31, 311–321.

151 B. Gyenes, D. A. Stevens, V. L. Chevrier and J. R. Dahn, J. Electrochem. Soc., 2015, 162, A278–A283.

152 F. Kong, R. Kostecki, G. Nadeau, X. Song, K. Zaghib, K. Kinoshita and F. McLarnon, J. Power Sources, 2001, 97–98, 58–66.

153 G. Jiang, L. Li, Z. Huang, Z. Xie and B. Cao, J. Alloys Compd., 2019, 790, 891–899.

154 R. Ramkumar and M. Minakshi, Dalt. Trans., 2015, 44, 6158–6168.

155 P. Sun, W. He, H. Yang, R. Cao, J. Yin, C. Wang and X. Xu, Nanoscale, 2018, 10, 19004–19013.

156 G. Xu, X. Ren, Z. Zhang, H. Zhang, X. Sun, X. Qi, P. Wan and Z. Huang, Nanoscale, 2016, 8, 13273–13279.

157 H. Liang, F. Meng, M. Cabán-Acevedo, L. Li, A. Forticaux, L. Xiu, Z. Wang and S. Jin, Nano Lett., 2015, 15, 1421–1427.

158 J. Xu, P. Gao and T. S. Zhao, Energy Environ. Sci., 2012, 5, 5333–5339.

159 Z. Liu, C. Yuan and F. Teng, J. Alloys Compd., 2019, 781, 460–466.

160 Q. Li, Y. Li, J. Zhao, S. Zhao, J. Zhou, C. Chen, K. Tao, R. Liu and L. Han, J. Power Sources, 2019, 430, 51–59.

161 J. Yi, Y. Qing, C. Wu, Y. Zeng, Y. Wu, X. Lu and Y. Tong, J. Power Sources, 2017, 351, 130–137.

162 L.-Q. Mai, F. Yang, Y.-L. Zhao, X. Xu, L. Xu and Y.-Z. Luo, Nat. Commun., 2011, 2, 381.

163 Z. Xu, Z. Li, X. Tan, C. M. B. Holt, L. Zhang, B. S. Amirkhiz and D. Mitlin, RSC Adv., 2012, 2, 2753–2755.

164 M. Mandal, D. Ghosh, S. Giri, I. Shakir and C. K. Das, RSC Adv., 2014, 4,

30832–30839.

165 K. Xu, J. Chao, W. Li, Q. Liu, Z. Wang, X. Liu, R. Zou and J. Hu, RSC Adv., 2014, 4, 34307–34314.

166 X. J. Ma, L. Bin Kong, W. Bin Zhang, M. C. Liu, Y. C. Luo and L. Kang, RSC Adv., 2014, 4, 17884–17890.

167 L. Jinlong, Y. Meng, K. Suzuki and H. Miura, Microporous Mesoporous Mater., 2017, 242, 264–270.

168 M. C. Liu, L. Bin Kong, C. Lu, X. J. Ma, X. M. Li, Y. C. Luo and L. Kang, J. Mater. Chem. A, 2013, 1, 1380–1387.

169 Z. Gu, R. Wang, H. Nan, B. Geng and X. Zhang, J. Mater. Chem. A, 2015, 3, 14578–14584.

170 J. Wang, J. Polleux, J. Lim and B. Dunn, J. Phys. Chem. C, 2007, 111, 14925–14931.

171 K. V. Sankar, Y. Seo, S. C. Lee, S. Liu, A. Kundu, C. Ray and S. C. Jun, Electrochim. Acta, 2018, 259, 1037–1044.

172 A. K. Singh, D. Sarkar, K. Karmakar, K. Mandal and G. G. Khan, ACS Appl. Mater. Interfaces, 2016, 8, 20786–20792.

173 S. T. Senthilkumar, N. Fu, Y. Liu, Y. Wang, L. Zhou and H. Huang, Electrochim. Acta, 2016, 211, 411–419.

174 T.-Y. Chen and L.-Y. Lin, Electrochim. Acta, 2019, 298, 745–755.

175 Y. Yuan, W. Wang, J. Yang, H. Tang, Z. Ye, Y. Zeng and J. Lu, Langmuir, 2017, 33, 10446–10454.

176 B. Deka Boruah, A. Maji and A. Misra, Nanoscale, 2017, 9, 9411–9420.

177 S. Baskar, D. Meyrick, K. S. Ramakrishnan and M. Minakshi, Chem. Eng. J., 2014, 253, 502–507.

APPENDIX: LIST OF PUBLICATIONS AND CONFERENCES

1. **Roshan Mangal Bhattarai**, Sudhakaran Moopri Singer Pandiyarajan, Shirjana Saud, Sang-Jae Kim, Young Sun Mok *- "*Synergistic effect of nanocarbon sphere sheathed on binderless $CoMoO_4$ electrode for high-performance asymmetric supercapacitor"*. Dalton Transactions. (Submitted).
2. Sudhakaran M.S.P., Gnanaselvan Gnanasekaran, Parthiban Pazhamalai, Surjit Sahoo, Md. Mokter Hossain, **Roshan Mangal Bhattarai,** Sang-Jae Kim, Young Sun Mok* **- "***Hierarchically Porous Nanostructured Nickel Phosphide with Carbon Particles Embedded by Dielectric Barrier Discharge Plasma Deposition as a Binder-Free Electrode for Hybrid Supercapacitors."*- ACS Sustainable Chem.
3. **Bhattarai Roshan Mangal**, MSP Sudhakaran, Md. M. Hossain, Saud Shirjana and Y.S. Mok- *"CoMoS@N-doped carbon nanocomposite as a high-performance anode material for lithium-ion batteries."*- CAEP-Vietnam, Oral presentation.
4. **Bhattarai Roshan Mangal**, Sudhakaran M.S.P, Md. Mokter Hossain, Saud Shirjana Young sun Mok- *"Application of Plasma to Fabricate Carbon Coated Ni2P Nano-composites for High Rate and High Stability Lithium Ion Batteries Anode Material"* KSIEC-Busan, Korea. Poster presentation.
5. **Bhattarai Roshan Mangal**, Sudhakaran M.S.P, Saud Shirjana, Young sun Mok- *"CoMoO4@N-doped Carbon Nanocomposite as a High-performance Anode Material for Lithium-ion Batteries."* ICMR-Jeju, Korea. Poster presentation.

6. Sudhakaran Moopri Singer Pandiyarajan, Gnanaselvan Gnanasekaran, Md. Mokter Hossain, **Roshan Mangal Bhattarai,** Young Sun Mok- *"Effective Use of Carbon Embedded Electrode by an Atmospheric DBD Plasma for Hybrid Supercapacitor."* ICMR-Jeju, Korea. Oral presentation.